The influence of back-arc extension direction on the strain partitioning associated with continental indentation: Analogue modelling and implications for the Circum-Moesian Fault System of South-Eastern Europe

Nemanja Krstekanić, Ernst Willingshofer, Liviu Matenco, Marinko Toljić, Uroš Stojadinović
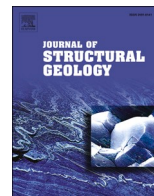
The influence of back-arc extension direction on the strain partitioning associated with continental indentation: Analogue modelling and implications for the Circum-Moesian Fault System of South-Eastern Europe | Nemanja Krstekanić, Ernst Willingshofer, Liviu Matenco, Marinko Toljić, Uroš Stojadinović | Journal of Structural Geology | 2022 | |

http://dr.rgf.bg.ac.rs/s/repo/item/0007246

The influence of back-arc extension direction on the strain partitioning associated with continental indentation: Analogue modelling and implications for the Circum-Moesian Fault System of South-Eastern Europe

Nemanja Krstekanić [a,b,*], Ernst Willingshofer [a], Liviu Matenco [a], Marinko Toljić [b], Uros Stojadinovic [b]

[a] *Utrecht University, Faculty of Geosciences, Utrecht, the Netherlands*
[b] *University of Belgrade, Faculty of Mining and Geology, Belgrade, Serbia*

ABSTRACT

Continental indentation is associated with deformation transfer from shortening to strike-slip faulting and is often affected by subduction related processes such as slab roll-back driven back-arc extension. We use crustal-scale analogue modelling to investigate the effects of extension direction on the strain partitioning and deformation transfer during indentation. The modelling results show that extension parallel to the strike-slip margin of the indenter creates subsidence distributed in several areas which may connect to form a large sedimentary basin behind the indenter. This transtensional basin with v-shape geometry narrows gradually towards the strike-slip margin of the indenter. In contrast, models with extension perpendicular to the strike-slip margin distributes transtensional deformation away from the indenter. Our results are in good correlation with the evolution of the Carpatho-Balkanides orocline of South-Eastern Europe, where the Circum-Moesian Fault System accommodates oroclinal bending during indentation against the Moesian Platform. In this area, the modelling explains the coeval and contrasting extensional features observed along the strike-slip margin and behind the indenter (i.e. the Getic Depression and the Morava Valley Corridor), driven by the roll-back of the Carpathian embayment and Adriatic slabs.

1. Introduction

Indentation is associated with a complex three-dimensional deformation transfer, different fault kinematics and strain partitioning during frontal shortening and lateral strike-slip deformation. Deformation is often associated with extrusion of continental fragments, observed in situations like India-Eurasia collision and SE Asia extrusion (Fig. 1a; e.g., Molnar and Tapponier, 1975; Morley, 2002, 2013; Searle et al., 2011; Shen et al., 2001; Tapponier et al., 1986), Arabia-Anatolia system (Fig. 1b; e.g., Kaymakci et al., 2010; Lyberis et al., 1992; Mantovani et al., 2006; Martinod et al., 2000; Perinçek and Çemen, 1990; Smit et al., 2010) or Adria-Europe convergence (Fig. 1c; e.g., Frisch et al., 1998; Neubauer et al., 2000; Ratschbacher et al., 1991b; Rosenberg et al., 2004; van Gelder et al., 2020; van Unen et al., 2019; Wölfler et al., 2011). In all these situations, indentation-induced deformation is affected by extension driven by the slab roll-back of another subduction zone (Fig. 1, see also Regard et al., 2005; Schellart et al., 2019; Sternai et al., 2016). This extension has a variable orientation (from parallel to perpendicular) with respect to the frontal shortening or the lateral strike-slip deformation taking place during indentation. The resulting multi-scale distribution of the bulk strain by connecting different kinematic types of deformation that cannot be explained by a uniform stress field is generally referred to as strain partitioning (e.g., Benesh et al., 2014; Cembrano et al., 2005; D'el-Rey Silva et al., 2011; De Vicente et al., 2009; Glen, 2004; Krézsek et al., 2013). Although it is known that slab-roll back can affect the large-scale deformation associated with indentation (e.g., Faccenna et al., 1996; Schellart et al., 2019), the mechanism of strain partitioning and deformation transfer between slab roll-back induced extension and indentation is not well understood. Previous research into indentation systems has demonstrated that the indenter geometry dominantly controls the strain partitioning and deformation transfer (Krstekanić et al., 2021), which should be accounted for when studying the impact of the extension driven by slab roll-back.

* Corresponding author. Utrecht University, Faculty of Geosciences, Utrecht, the Netherlands.
E-mail address: n.krstekanic@uu.nl (N. Krstekanić).

We aim to understand the interplay of extension driven by slab roll-back and indentation-driven deformation, together with a quantification of the associated strain partitioning and fault kinematics. To this aim, we performed crustal-scale analogue modelling experiments designed to test the influence of the extension direction during indentation in terms of kinematics, distribution of deformation and the coeval formation and evolution of sedimentary basins. Image correlation methods were used to qualitatively and quantitatively analyse deformation patterns around the indenter. The analogue experiments were scaled and applied to the indentation of the Moesian Platform during the formation of the arcuate back-arc convex Carpatho-Balkanides orocline that was coeval with the back-arc extension driven by the Carpathian embayment and Adriatic slabs (Fig. 2).

2. The Circum-Moesian Fault System of the Carpatho-Balkanides

The Carpatho-Balkanides orogenic system of South-Eastern Europe (Fig. 2a) is a Cretaceous thick-skinned nappe stack whose formation was associated with the closure of the Ceahlău-Severin branch of the Alpine Tethys Ocean leading to the collision between the Dacia mega-unit and the Moesian Platform, a promontory of the stable pre-Alpine European continent (Fig. 2a and b; Săndulescu, 1988; Csontos and Vörös, 2004; Schmid et al., 2008, 2020). Subsequent Cenozoic subduction, slab retreat and closure of the Carpathian embayment created the oroclinal bending and the present-day double 180° curved geometry of the entire orogenic system (Fig. 2a; e.g., Csontos and Vörös, 2004; Fügenschuh and Schmid, 2005; Ustaszewski et al., 2008).

The southern part of the double 180° orocline consists of the South Carpathians, the Serbian Carpathians and the Balkanides and has a backarc-convex geometry (Krstekanić et al., 2020) formed by oroclinal bending and dextral transcurrent motions of the Dacia mega-unit around the Moesian Platform (Fig. 2b; van Hinsbergen et al., 2020). This oroclinal bending was first accommodated by Paleocene – Eocene orogen-parallel extension in the South Carpathians (Matenco and Schmid, 1999; Fügenschuh and Schmid, 2005; Schmid et al., 1998), followed by Oligocene-middle Miocene deformation along the Circum-Moesian Fault System (thick black lines in Fig. 2b), one of the largest European intracontinental strike-slip fault systems, accumulating up to 140 km of dextral offset, associated with coeval thrusting and normal faulting (e.g., Krstekanić et al., 2022). These faults have different orientations, connect and transfer the deformation along the entire orocline, from the South Carpathians in the north to the Balkanides in the south. The largest faults in the system are the Cerna and Timok curved strike-slip faults that have 35 km and 65 km of dextral offset, respectively, and connect with thrusting-dominated deformation in the frontal part of the South Carpathians and Balkan Mountains (Fig. 2b; see also Berza and Drăganescu, 1988; Ratschbacher et al., 1993; Kräutner

and Krstić, 2002).

The evolution of the Circum-Moesian Fault System was (partly) coeval with widespread extensional processes related to the roll back of the Carpathian embayment and Adriatic slabs (Bennett et al., 2008; Matenco and Radivojević, 2012; Horváth et al., 2015, Andrić et al., 2018) where the latter probably controlled E-W extension in the Morava Valley Corridor, the southern prolongation of the Pannonian Basin, and affected the western margin of the Serbian Carpathians segment of the orocline, from Oligocene to middle Miocene times (Figs. 1c and 2a; Matenco and Radivojević, 2012; Erak et al., 2017; Sant et al., 2018; Krstekanić et al., 2020). Additionally, the oroclinal bending was complicated by one other extensional/transtensional deformation that affected the Serbian and South Carpathians during their movement around the Moesian indenter and the formation of the Circum-Moesian Fault System, driven by the Carpathian embayment slab roll-back kinematics (Figs. 1c and 2). In the prolongation of the Timok Fault (Fig. 2b), a late Oligocene – early Miocene period of transtension and extension led to the opening of the Getic Depression in the South Carpathians foreland, which was subsequently inverted and buried during the middle to late Miocene docking of the South Carpathians against the Moesian indenter (e.g., Matenco et al., 2003; Răbăgia et al., 2011; Krézsek et al., 2013). This extension also created a number of presently E-W oriented intra-montane basins in the Serbian Carpathians (Krstekanić et al., 2020, 2022). These complex movements around the Moesian indenter are inferred to be driven by rotational kinematics of the retreating Carpathian embayment slab and the formation of a STEP (subduction-transform edge propagator) system at high depths beneath the South Carpathians (Fig. 2a; Govers and Wortel, 2005; Maţenco, 2017).

3. Methodology

Starting from a published analogue modelling setup with a fixed indenter, around which a deformable material is translating and rotating (Krstekanić et al., 2021), we have performed crustal scale analogue experiments to simulate deformation in the upper to middle crust around a rigid indenter under the influence of variable extension direction. We note that the unusual high complexity of strain partitioning requires a correlation with this previously published study. Our experiments are designed (Fig. 3) to simulate the impact of the variability in kinematic boundary conditions and provide the possibility of a direct analysis of deformation styles. Four different kinematic setups were chosen to compare the deformation transfer and strain partitioning for cases with and without an externally-driven extension affecting the indentation process. The applied extension was either N–S (model 2), E-W (model 3) or coevally in both directions (model 3), consistent with the observed extension directions that affect the Carpatho-Balkanides
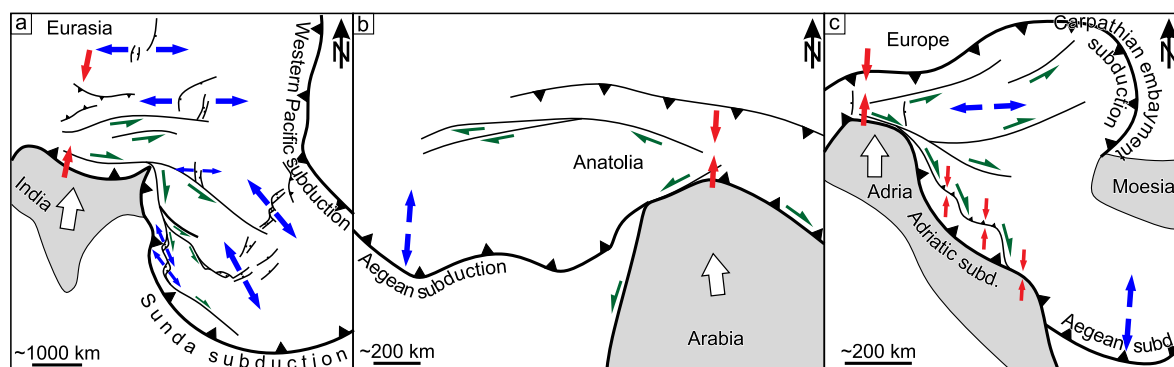
Fig. 1. Sketches of natural indentation systems. a) India – Eurasia collision. b) Arabia indentation and lateral extrusion of Anatolia. c) Adria – Europe collision. Indenters are grey areas. White arrow shows direction of indenter motion. Triangles along contractional zones are drawn in the upper plate/hanging wall of a subduction/thrust. Green half arrows indicate kinematics along strike-slip faults. Red arrows indicate shortening regions, while blue arrows indicate extension. (For interpretation of the references to colour in this figure legend, the reader is referred to the Web version of this article.)

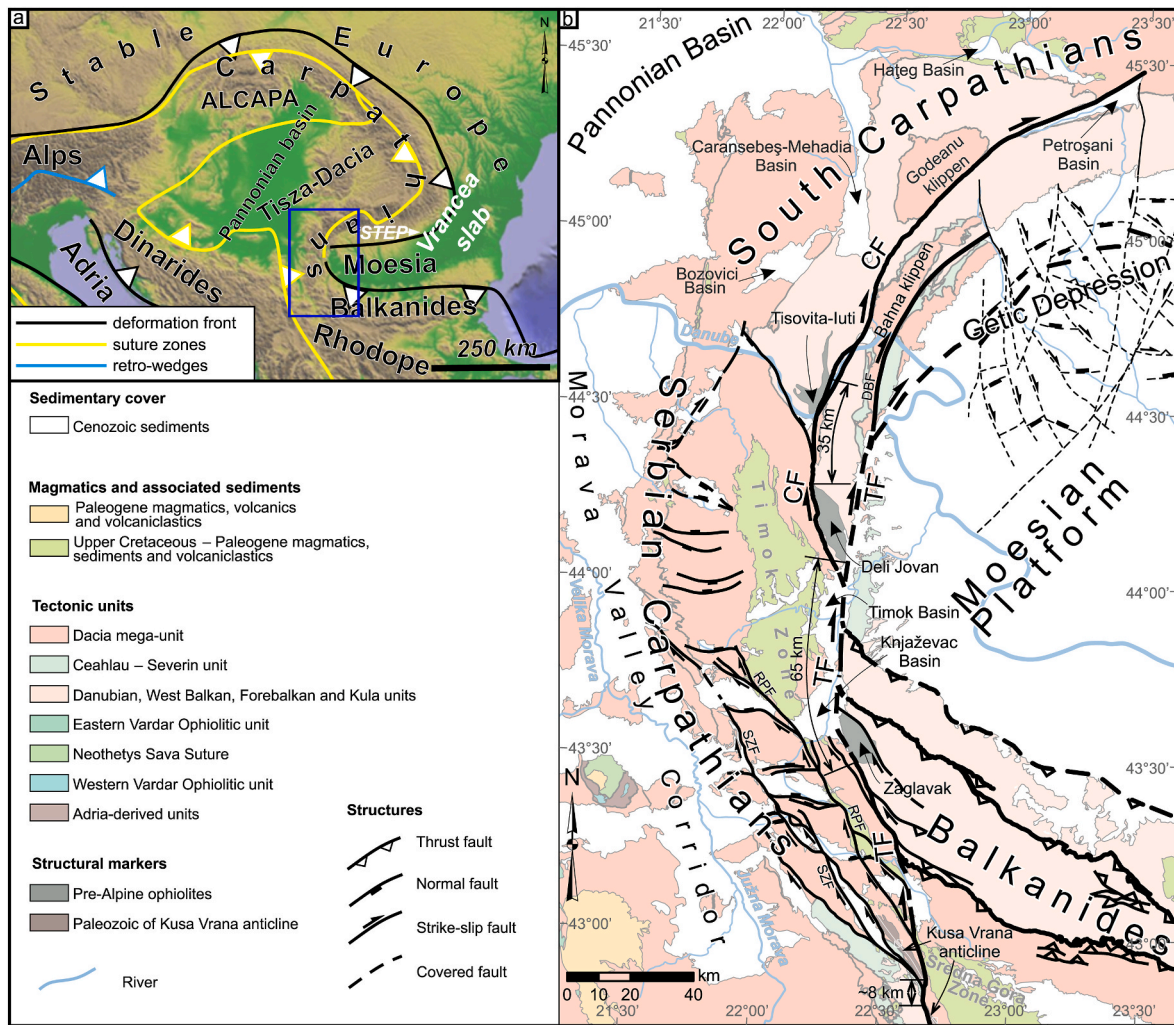**Fig. 2.** a) First-order structures (orogenic fronts, suture zones and retro-shears) of the Mediterranean Alpine-age orogens in South-Eastern Europe (modified from Krstekanić et al., 2020). Blue rectangle indicates the location of Fig. 2b. STEP – Subduction-Transform Edge Propagator system in the South Carpathians. White arrow indicates the direction of slab tearing. b) Tectonic map of the South Carpathians-Serbian Carpathians-Balkanides backarc-convex orocline around the Moesian Platform. Black lines are faults comprising the Circum-Moesian Fault System that accommodates oroclinal bending related deformation. CF – Cerna Fault; TF - Timok Fault. The map is compiled and modified after geological maps of Serbia, Romania and Bulgaria and Maţenco (2017). Fault pattern is modified after Maţenco (2017) and Krstekanić et al. (2022). (For interpretation of the references to colour in this figure legend, the reader is referred to the Web version of this article.)

orocline in its South Carpathians and Serbian Carpathians segments (e. g., Răbăgia et al., 2011; Krstekanić et al., 2022). Below we describe the modelling setup and results in a relative geographic framework where north is oriented upwards in top-view figures (e.g., Fig. 3), in analogy to the geographic framework of the Circum-Moesian Fault System (Fig. 2).

3.1. Modelling setup

3.1.1. Model geometry and kinematics

The indenter is made of a 2 cm thick rigid polyvinyl chloride plate with rounded corners (Figs. 3a) and 35° margin inclination (Fig. 3c), approximating the geometry of the base of the Cretaceous nappe-stack thrust over the Moesian Platform (Fig. 2b; Maţenco, 2017 and references therein). The indenter upper width of 26 cm (Fig. 3a) correlates with the N–S dimension of the Moesian Platform (Fig. 2).

Similar to Krstekanić et al. (2021), the base of the deformable part of models is made of a mobile basal plastic plate and a fixed plastic sheet (Fig. 3). The 1 mm thick plastic plate (green in Fig. 3) underlies the entire model, including the rigid block. Through a bar and mechanical joints it is connected to a motor (Fig. 3a) that pulls it northward at a constant velocity of 2 cm/h. The other, fixed 0.1 mm thick plastic sheet

(grey in Fig. 3) is placed on top of the moving plate north of the indenter, while it is below the moving plate to the north-west. This change is implemented at the N–S oriented cut in the middle of the moving plate (dashed green line in Fig. 3a). The purpose of this configuration is to prevent an E-W oriented velocity discontinuity along the northern margin of the indenter. This setup pre-defines velocity discontinuities (VD) in all models along the southern and western margins, as well as along the south-western corner of the indenter and along the cut in the moving plastic plate in the north (Fig. 3a).

The mobile plastic plate moves north-wards in all models and its movement is controlled by the fixed guide bar in the north (Fig. 3a), which results in a coupled translational and rotational movement (Fig. 3b). The rotational component of motion is controlled by a stationary pin protruding from below the indenter (fixed pin in Fig. 3a), creating a pole of rotation. The cut in the moving plastic plate enables its sliding and rotation around the stationary pin. The coupled translation and rotation takes place during the entire period of each experiment, resulting in the total northward displacement of the mobile plate of 9 cm and 10° of clockwise rotation (Fig. 3b).

The difference between our models is the change in kinematic boundary conditions applied to the northern and western margins of the
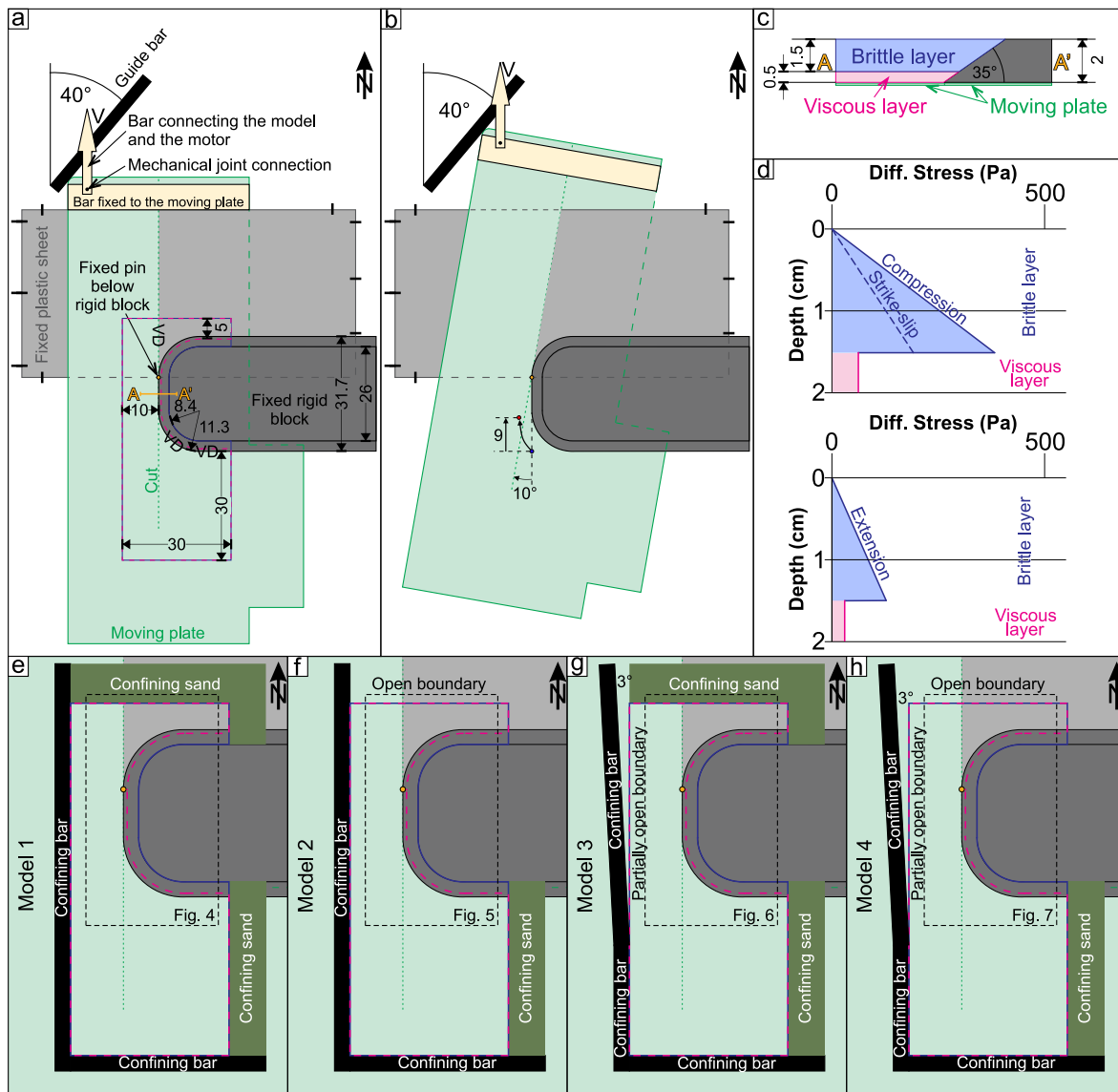
Fig. 3. Modelling setup. All numbers without units in Fig. 3a–c are in centimetres. a) Initial models' geometry setup and dimensions. b) Configuration of the basal plastic plate/sheet at the end of each experiment. Complex movement of the moving plate includes coupled north-ward translation and clockwise rotation that result in a total of 9 cm of north-ward translation and 10° of rotation (blue to red circle). c) Simplified sketch of setup cross-section. Cross-section location is indicated in Fig. 3a d) Strength profiles for all models. For calculating strength of the viscous layer we used mean PDMS viscosity of 2.8 Pa s at 20 °C measured by Rudolf et al. (2016). e-h) Kinematic boundary conditions applied to model boundaries for each of the four models presented in this study. The confined boundary indicates that any flow of the viscous layer is prevented at that boundary, while the open boundary allows gravity-driven flow of the viscous layer in a direction perpendicular to the boundary. Dashed black lines indicate areas of the models shown in Figs. 4–7. (For interpretation of the references to colour in this figure legend, the reader is referred to the Web version of this article.)

model, simulating different effects of extensional directions on the deformation transfer around the indenter. In model 1 (Fig. 3e) all model boundaries are confined, either by metal bars or sand, to prevent the silicone putty (see material properties below) flowing and creating extension. The effect of extension is simulated in models 2, 3 and 4 by (partially) opening lateral boundaries in the northern, north-eastern and western parts of the models, which allows for extension of the model by gravity driven flow of the viscous, silicone putty layer in direction perpendicular to the open boundary. For loading conditions applied in this study, the gravity driven average velocity of the flow is ~9.6 mm/h (see also section 3.2). Model 2 (Fig. 3f) has open northern and north-eastern boundaries, which facilitates the flow of the viscous layer away from the indenter (i.e., to the north and north-east). Model 3 (Fig. 3g) has a partially open western boundary and allows the silicone putty to flow to the west until it reaches a confining bar, which is at a

larger distance in the north compared to the south (Fig. 3g) introducing a displacement gradient which simulates the limited extension of the south-ward narrowing Morava Valley Corridor. In model 4 (Fig. 3h) the northern boundary is fully open (as in model 2) and the western boundary is open partially (as in model 3).

3.1.2. Model materials

All four models consist of brittle and viscous layers with the same rheological properties (Fig. 3a–d). The 1.5 cm thick brittle layer is made of dry feldspar sand with a bulk density of $\rho = 1300 \text{ kg/m}^3$, a cohesion of 10–50 Pa and coefficients of friction of 0.68, 0.55 and 0.61, representing peak, dynamic and reactivation friction, respectively (Willingshofer et al., 2005, 2018). The sand has been sieved to the grain size of 100–250 μm. Thin marker horizons of black feldspar sand mark vertical offsets along faults in cross-sections. Horizontal offsets are shown by

passive maker lines of black and pink feldspar sand placed on the model's top surface. In Fig. 3a, the outline of the sand layer in the model is shown with a blue line and where it is in contact with the indenter it coincides with the upper edge of the inclined indenter margin (Fig. 3a, c).

Underlying the feldspar sand, the 0.5 cm thick viscous layer (pink dashed outline in Fig. 3a, see also Fig. 3c) is analogous to the ductile crust below the brittle-ductile transition. It is made of poly-dimethylsiloxane (PDMS silicone polymer) putty that has a Newtonian behaviour for strain rates below 10^{-1} s^{-1} (Rudolf et al., 2016), with a density of $\rho = 970$ kg/m^3, no yield strength and an average viscosity of $2.8 \ 10^4$ Pa s at room temperature ($\sim$20 °C; Rudolf et al., 2016).

3.2. Scaling

We scaled our models to nature according to principles of geometrical, rheological and kinematical similarities (Hubbert, 1937; Ramberg, 1981; Weijermars and Schmeling, 1986; Davy and Cobbold, 1991). When scaling lengths, we follow the previous analogue modelling study applied to the same natural case of the Carpatho-Balkanides by Krstekanić et al. (2021). This means that 1 cm in our models corresponds to 7 km in nature, which yields a length-scale ratio L* $= 1.43 \bullet 10^{-6}$. With this length-scale ratio, 1.5 cm depth of the brittle-viscous transition in our models corresponds to $\sim$10 km depth in nature, which is supported by the shallow seismicity and the crustal structure reported in the South and Serbian Carpathians (e.g., Dimitrijevic, 1994; Popa et al., 2018). Lithostatic stress at this depth in the experiments is 191 Pa, which corresponds to 280 MPa in nature, resulting in a stress-scale ratio of $6.82 \bullet 10^{-7}$. Such stress conditions at the base of the brittle layer lead to a threefold increase of flow velocity of silicone as determined by separate gravity driven flow test, performed under loaded (1.5 cm feldspar sand on top of the silicone layer) and not loaded conditions. Following Brun (2002) strength profiles (Fig. 3d) have been calculated, which are representative for the initial model conditions. Externally imposed velocity, controlled by the engine, was used to calculate strength profiles for the strike-slip and compression regimes, whereas we used flow velocity of silicone putty under loaded conditions to calculate the strength of the viscous layer under gravity driven extension. Based on the flow properties of the viscous layer, we scaled velocity in our models for the strike-slip deformation, following Krstekanić et al. (2021), by calculating a time-scale ratio (Hubbert, 1937) t* $= 5.3 \bullet 10^{-11}$, which yields a velocity ratio V* $= 2.7 \bullet 10^4$. It follows that a velocity of 2 cm/h in our models scales to 0.65 cm/yr in nature. This corresponds well with the 60–65 km displacement along the Timok Fault during $\sim$10 Myr (Kräutner and Krstić, 2003; Schmid et al., 2020). Though the velocity scaling is tied to the strike-slip deformation, we note that the displacement rates along normal faults in the Getic Depression (0.4–0.6 mm/y during the period of activity of the Timok Fault, estimated from normal fault offsets reported in Krézsek et al., 2013 and references therein) are significantly lower compared to the strike-slip faults (e.g., Krézsek et al., 2013). This correlates well with gravity driven and engine driven flow velocities in our models, although the difference between the two velocities in our models is lower than those in nature.

3.3. Experimental procedures, monitoring and analysis approach

All models are built and run in a normal gravity field and at room temperature ($\sim$20 °C). During the experiment, extensional deformation creates depressions in models. In order to track deformation in these depressions (i.e., basins), when they become $\sim$1 mm deep, we fill them with alternating layers of differently coloured sand using a funnel. This sand represents, in a simplified way, syn-kinematic sedimentation. To preserve topography at the end of each experiment, two post-kinematic layers of black and white sand are sieved on top to cover the entire model. Subsequently, water is sprinkled on the sand layers to increase cohesion in the sand allowing for sectioning of the experiments in order

to obtain information on the geometry of deformation structures.

Top-view photographs perpendicular to the model surface are taken at regular time intervals of 3 min, which corresponds to 0.1 cm of motor-induced northward displacement between two photographs. We use particle image velocimetry on these top-view photographs (PIVlab, Thielicke and Stamhuis, 2014) to calculate incremental particle displacements for each pair of adjacent photographs in the time series. The obtained incremental displacement fields are inspected for the presence of very large displacements that represent data outliers. Such outliers form due to incorrect correlations and are removed by applying a magnitude threshold filter, followed by visual inspection and manual removal. Displacements in basins for time frames when syn-kinematic sedimentation is added cannot be correlated automatically. Therefore, for these few time frames in each model, displacements in basin areas are interpolated from basin margins. Displacement fields are further analysed using the methodology and Strain Map software of Broerse et al. (2021) and Broerse (2021) to calculate 2D average strain type at the surface during evolution of our models. In the end, we combine our 2D strain analysis with visual interpretation of top-view photographs and vertical-cross sections to infer 3D deformation in our models.

3.4. Modelling limitations and simplifications

The laboratory time-scale of our experiments is 5 h during which deformation is induced by horizontal motion of a mobile plate as described in section 3.1.1. This relatively fast deformation allows for adopting an inverse density gradient of the model layers without influencing the modelling outcome. This simplification is justified because buoyancy driven vertical motions typically occur on laboratory time-scales of days (e.g., Cobbold and Szatmari, 1991; Brun and Fort 2004, 2011; Krézsek et al., 2007; Warsitzka et al., 2015). Additionally, salt tectonic experiments have shown that syn-kinematic sedimentation significantly reduces diapirism even on longer time-scales (e.g., Krézsek et al., 2007; Brun and Fort 2011). We, therefore, consider that the buoyancy effect is negligible in our models and that no diapirism contributed to the overall deformation.

Furthermore, our models do not account for isostasy, surface erosion and sediment transport, creating exaggerated topography in the contractional area in front of the indenter. However, this area is not the main target of our study as we focus more on the interaction between strike-slip and extension behind the indenter and along its lateral margin. As our models do not account for vertical temperature gradients, the viscosity of the silicone putty simulating viscous behaviour is constant with depth, which is considered acceptable in analogue modelling studies (e.g., Davy and Cobbold, 1991). All other simplifications follow Krstekanić et al. (2021).

4. Results

The modelling results are presented as top-view photographs and average strain maps (Fig. 4 – 7) for key moments in the evolution of all 4 models (i.e., after 1 cm, 4 cm and 9 cm of northward displacement) and interpreted cross-sections (Figs. 4–7) portraying the final deep structure of each experiment. Furthermore, time-lapse map-view videos of each model (see Supplementary material) were used to derive kinematics and temporal and spatial evolution of fault pattern during deformation.

4.1. Model 1: reference model with closed boundaries

In this experiment, all sides are confined by metal bars or sand and the model shows a gradual transition from dextral strike-slip dominated deformation along the western indenter's margin through transpression around the indenter's SW corner to shortening-dominated deformation along the southern margin (Fig. 4). The evolution of this deformation transfer and fault pattern is gradual and increases its complexity through time.
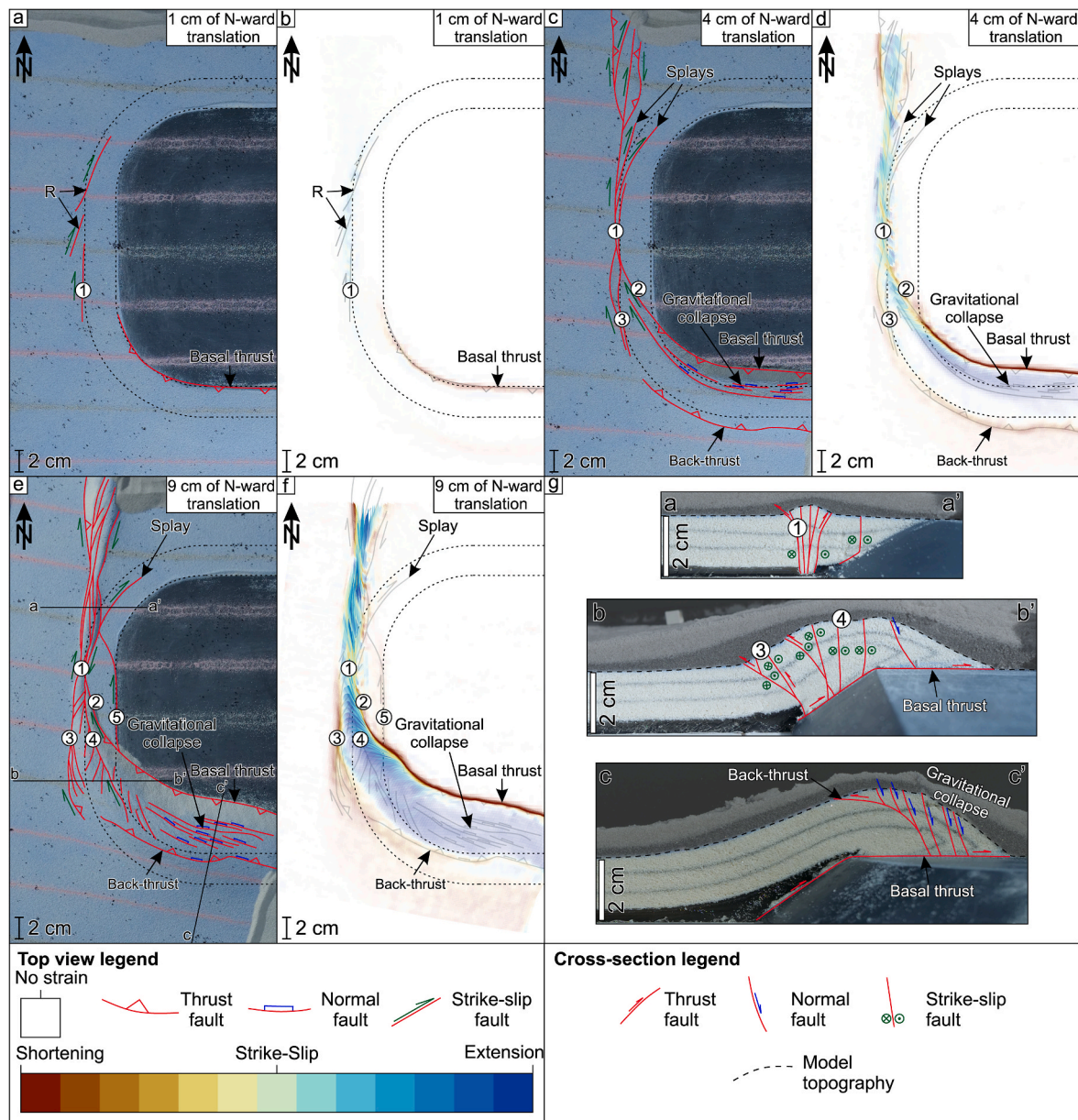
Fig. 4. Model 1 - closed boundaries. Dashed black lines mark the upper and lower edges of the indenter. R – Riedel shear. a) Interpreted top-view photo after 1 cm of north-ward translation. b) Cumulative average strain type map after 1 cm of north-ward translation. c) Interpreted top-view photo after 4 cm of north-ward translation. d) Cumulative average strain type map after 4 cm of north-ward translation. e) Interpreted top-view photo at the end of the experiment. f) Cumulative average strain type map at the end of the experiment. Strain plots in Fig. 4b, d and f overlay visually interpreted structures from Fig. 4a, c and e (grey lines). Strain colour legend corresponds to Fig. 4b, d and f. Note that in order to suppress areas without significant deformation, the transparency of areas with a strain magnitude below the 90 percentile is increased. g) Cross-sections of the reference model at the end of the experiment. Dashed line marks the model topography at the end of the experiment. Shaded area in the upper part of each cross-section marks post-kinematic sand cover. Cross-section locations are shown in Fig. 4e. (For interpretation of the references to colour in this figure legend, the reader is referred to the Web version of this article.)

Early in the deformation history, lateral movement along the western indenter margin is accommodated by en-échelon NNE-SSW oriented Riedel shears (R in Fig. 4a, b) and a N–S oriented strike-slip fault, which develops above the lower edge of the indenter's margin (1 in Fig. 4a and b). At the same time shortening south of the indenter is accommodated along the top-N basal thrust (Fig. 4a and b), which has no clear connection to the strike-slip faults.

After approximately 4 cm of total northward translation (Fig. 4c and d), strike-slip fault segments connect to form a through-going N–S oriented fault system (1 in Fig. 4c and d). North of the pole of rotation, this strike-slip system partitions deformation in a positive flower structure with shortening to transpression being accommodated along the

margins of the system (red and orange in Fig. 4d) and strike-slip to transtension (green and light blue in Fig. 4d) in the centre of the deformation zone. Remnants of Riedel shears form NNE oriented curved splays within the strike-slip system (Fig. 4c and d). The strike-slip system transfers part of its offset south-east-wards to a basal thrust via transpressional NW-SE oriented faults (2 in Fig. 4c and d), during its gradual south-wards propagation (3 in Fig. 4c and d). Shortening in front of the indenter is also accommodated by a new back-thrust (Fig. 4c and d) and weak, distributed shortening farther to the south (pale red in Fig. 4d). In the area between the basal thrust and the back-thrust, minor extensional deformation (blue in Fig. 4d) accommodates the change from ramp to upper-flat surface of the indenter.

The first order style and kinematics of deformation remain similar until the end of experiment (i.e., after 9 cm of total northward translation; Fig. 4e and f), especially in the north, where the positive flower structure and north-east-ward splay remain with a similar geometry and strain pattern (Fig. 4e and f and cross-section a-a' in Fig. 4g). To the south, the connection between the main strike-slip fault (1 in Fig. 4e and f) and the basal thrust remains active and linked up with the NW-SE transpressional fault (2 in Fig. 4e and f). A new complex strike-slip fault (4 in Fig. 4e and f and cross-section b-b' in Fig. 4g) with numerous low-offset splays propagates south-wards from the main strike-slip system and deforms the previously formed thrust wedge.

South of the indenter, weak extensional deformation with numerous low-offset normal faults partially reactivates the back-thrust, while the bulk shortening is accommodated along the basal thrust (Fig. 4e and f, and cross-section c-c' in Fig. 4g).

4.2. Model 2: open northern boundary

The open northern boundary in model 2 creates extension, which results in the opening of a large fault-controlled extensional basin north of the indenter (highlighted semi-transparent white area in Fig. 5a, c, e). This basin reflects the interplay between extension and strike-slip
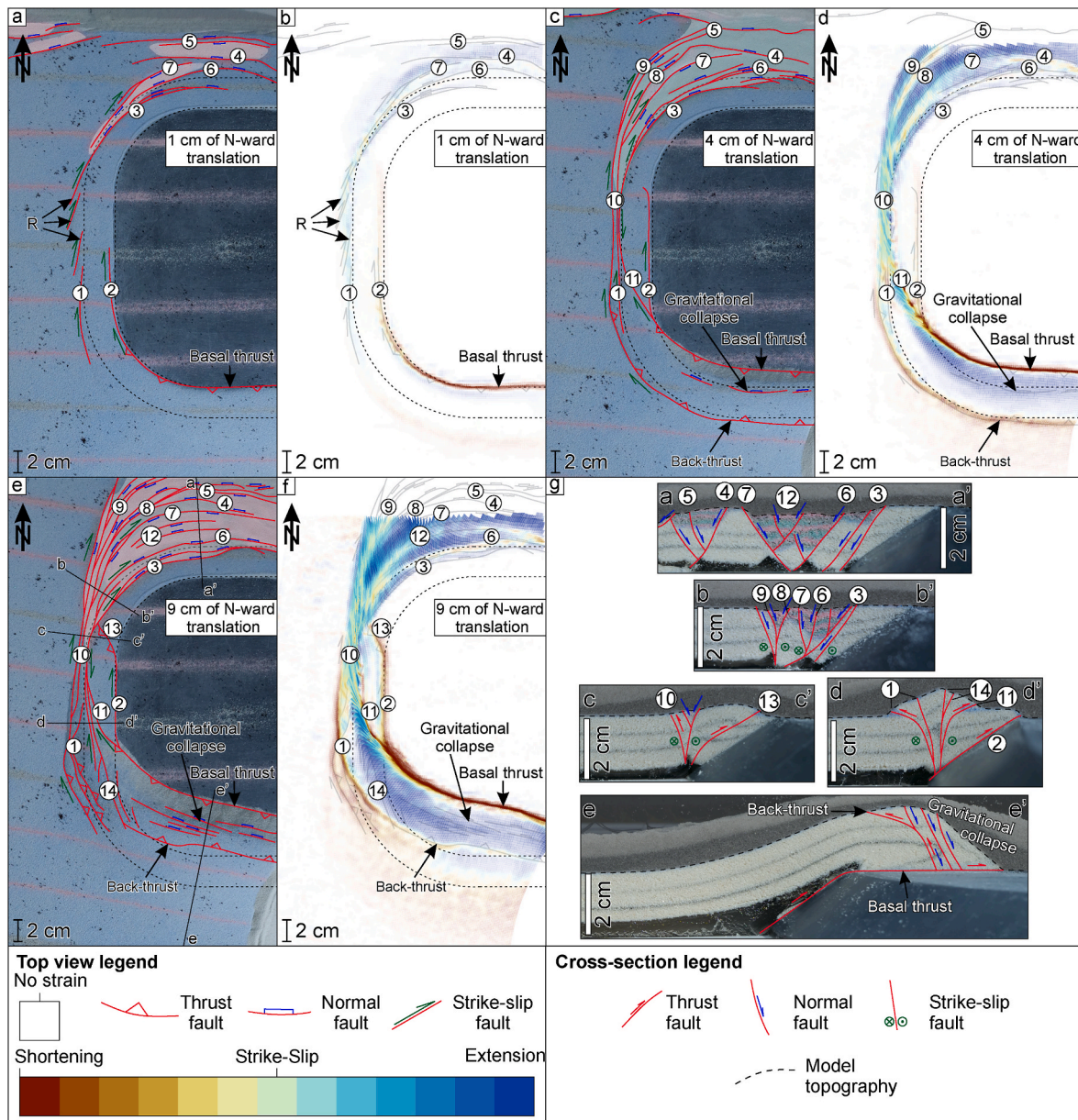

Fig. 5. Model 2 - open northern boundary. Dashed black lines mark the upper and lower edges of the indenter. R – Riedel shear. Highlighted semi-transparent white area marks the location of basin(s) with sedimentary infill. a) Interpreted top-view photo after 1 cm of northward translation. b) Cumulative average strain type map after 1 cm of northward translation. c) Interpreted top-view photo after 4 cm of northward translation. d) Cumulative average strain type map after 4 cm of northward translation. e) Interpreted top-view photo at the end of the experiment. f) Cumulative average strain type map at the end of the experiment. Strain plots in Fig. 5b, d and f overlay visually interpreted structures from Fig. 5a, c and e (grey lines). Strain colour legend corresponds to Fig. 5b, d and f. Note that in order to suppress areas without significant deformation, the transparency of areas with a strain magnitude below the 90 percentile is increased. g) Cross-sections of the reference model at the end of the experiment. Dashed line marks the model topography at the end of the experiment. Shaded area in the upper part of each cross-section marks post-kinematic sand cover. Cross-section locations are shown in Fig. 5e. (For interpretation of the references to colour in this figure legend, the reader is referred to the Web version of this article.)

deformation because the entire fault system north of the indenter connects towards SW to the N–S oriented dextral strike-slip deformation. This strike-slip system further transfers deformation to thrusting on top of the southern indenter's margin. The latter feature has the same evolution, geometry and kinematics as in the model 1 for the entire experiment duration (Fig. 5).

The early strike-slip deformation along the western indenter's margin is accommodated by NNE-SSW oriented Riedel shears (R in Fig. 5a and b) and early N–S oriented strike-slip faults (1 and 2 in Fig. 5a and b). To the south, fault 2 connects to the basal thrust, while to the north, Riedel shears connect to numerous normal faults that

accommodate extensional deformation (3–7 in Fig. 5a and b). These normal faults dip either to the north or south creating small and isolated basins (e.g., between faults 6 and 7 and 4 and 5 in Fig. 5a) separated by ridges (such as between faults 4 and 7 in Fig. 5a, cross-section a-a' in Fig. 5g). Closer to the indenter, these normal faults have curved geometries (3, 6 and 7 in Fig. 5a), controlled by the NW indenter corner, as they gradually transfer extension through transtension to strike-slip deformation (Fig. 5b).

After 4 cm of northward translation, the strike-slip system is fully connected into a continuous multi-strand structure (10 and 11 in Fig. 5c and d). In the north, the small, early basins connect into a single larger
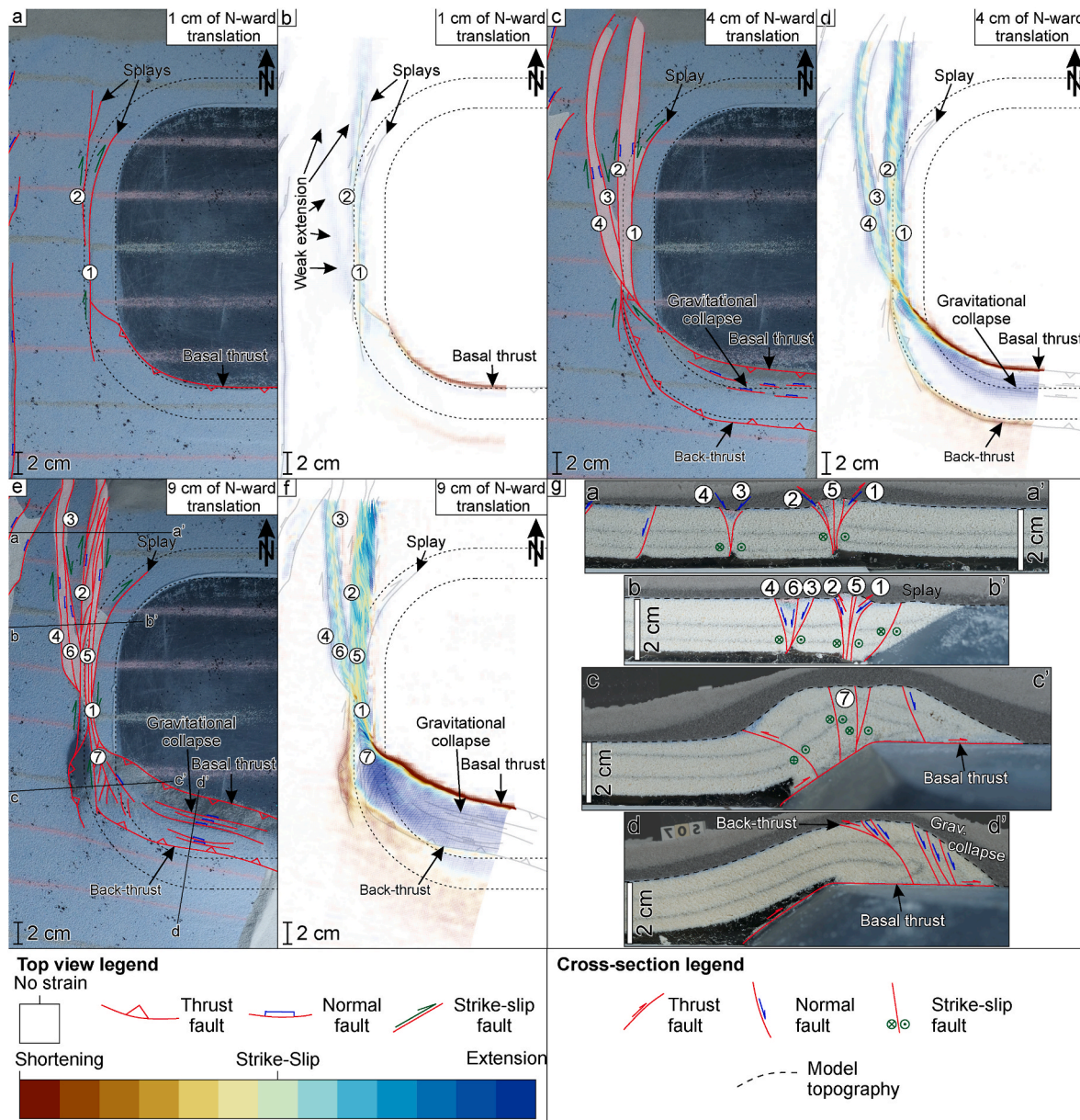

Fig. 6. Model 3 - partially open western boundary. Dashed black lines mark the upper and lower edges of the indenter. R – Riedel shear. Highlighted semi-transparent white area marks the location of basin(s) with sedimentary infill. a) Interpreted top-view photo after 1 cm of northward translation. b) Cumulative average strain type map after 1 cm of northward translation. c) Interpreted top-view photo after 4 cm of northward translation. d) Cumulative average strain type map after 4 cm of northward translation. e) Interpreted top-view photo at the end of the experiment. f) Cumulative average strain type map at the end of the experiment. Strain plots in Fig. 6b, d and f overlay visually interpreted structures from Fig. 6a, c and e (grey lines). Strain colour legend corresponds to Fig. 6b, d and f. Note that in order to suppress areas without significant deformation, the transparency of areas with a strain magnitude below the 90 percentile is increased. g) Cross-sections of the reference model at the end of the experiment. Dashed line marks the model topography at the end of the experiment. Shaded area in the upper part of each cross-section marks post-kinematic sand cover. Cross-section locations are shown in Fig. 6e. (For interpretation of the references to colour in this figure legend, the reader is referred to the Web version of this article.)

basin with intra-basinal highs and sub-basins, while new faults (e.g., 8 and 9 in Fig. 5c and d) form to connect normal faults with the strike-slip system along the western indenter's margin.

Towards the end of the experiment, the basin system in the north further enlarges with new smaller normal faults forming within its interior (e.g., 12 in Fig. 5e and f, cross-section a-a' in Fig. 5g). The overall strain pattern north of the indenter shows intercalating regions of extension-dominated and strike-slip to transtension-dominated deformation. The latter are more frequent around the NW indenter corner where the basin is narrower and extension connects with strike-slip system (Fig. 5f, cross-section b-b' in Fig. 5g). Along the western indenter's margin, fault 2 propagates to connect with the main strike-slip system along an oblique thrust (13, Fig. 5e and f, cross-section c-c' in Fig. 5g). To the south, the main strike-slip system (10 in Fig. 5e and f) completely inverts the narrow southern tip of the basin (cross-section c-c' in Fig. 5g), creating a positive topography (cross-section d-d' in Fig. 5g) during its south-ward propagation (14 in Fig. 5e and f).

4.3. Model 3: partially open western boundary

The ~ E-W extension induced along the western model margin creates a distinctively different fault pattern along the western indenter margin compared to the previous two models (Fig. 6), where strain is partitioned into two sub-parallel ~ N–S oriented zones of combined dextral strike-slip, transtension and extension. To the south, strike-slip deformation is transferred to thrusting on top of the southern indenter's margin, which creates the same deformation pattern as in the previous two models.

The early-stage deformation is localized in two closely spaced, sub-parallel dextral strike-slip faults (1 and 2 in Fig. 6a and b), also associated with a weak extensional strain (blue in Fig. 6b). North-wards, these two faults splay to form NE striking faults around the indenter's NW corner (Fig. 6a and b).

The evolution of both strike-slip and E-W oriented extension leads to formation of two separate deformation zones, which connect where strike-slip deformation is gradually replaced by transpressive deformation at the southwestern indenter corner (Fig. 6c and d). The eastern of the two forms on top of the velocity discontinuity and is controlled by faults 1 and 2 (Fig. 6c and d), while the western deformation zone is slightly younger and is controlled by faults 3 and 4 (Fig. 6c and d). In both zones, subsidence in narrow basins (Fig. 6c) is controlled by dominant dip-slip faults, while strike-slip deformation affects central areas of the basins (Fig. 6d).

With progressing deformation, new faults with dominant strike-slip kinematics form within the two deformation zones (e.g., faults 5 and 6 in Fig. 6e and f). The gradual cessation of extension along the western model margin leads to basins inversion, mostly along the eastern shear zone. This is, for instance, observed in cross-sections a-a' and b-b' (Fig. 6g) where positive topography in the basin area (between faults 1 and 2), the offset at the base of the basin and deformed sedimentary infill indicate inversion of originally transtensive faults (1 and 2) and new strike-slip faulting (5). Strike-slip deformation becomes subsequently the dominant deformation along the western indenter's margin, where it propagates south-wards and overprints the earlier thrust wedge (e.g., fault 7 in Fig. 6e and f and cross-section c-c' in Fig. 6g). The thrust wedge (cross-section d-d' in Fig. 6g) displays the same structural pattern as in models 1 and 2 (cross section c-c' in Fig. 4g and cross-section e-e' in Fig. 5g) where most of thrusting is accommodated along the basal thrust, while a single back-thrust is reactivated by low-offset normal faulting.

4.4. Model 4: open northern and partially open western boundaries

The coevally evolving extensions along the northern and western model margins create a large extensional basin north of the indenter, which shows a combination of features observed in models 2 and 3. Extension is gradually transferred to dextral strike-slip and transtension

that affects a wide area along the western margin of the indenter. South-wards, the strike-slip deformation is transferred to shortening like in all previous models (Fig. 7).

Early in the model evolution, the deformation along the western indenter's margin is accommodated by two N–S oriented dextral trans-tensional faults (1 and 2 in Fig. 7a and b), which control a narrow basin in between. Distributed subsidence affects a wider area west of these two faults (blue in Fig. 7b), with no evident normal faulting at the resolution of the model. North-wards, strike-slip to transtensional faults curve around the NW indenter's corner to connect to transtensional to normal faults north of the indenter (3–8 in Fig. 7a and b). These normal faults dip north-wards or south-wards, creating several isolated basins (Fig. 7a, see also cross-sections a-a' and b-b' in Fig. 7g).

After ~4 cm of north-ward translation, the isolated basins and intervening highs are connected into one large basin (Fig. 7c and d, see also cross-section a-a' in Fig. 7g). This basin enlargement and connection with strike-slip deformation takes place along previously and newly formed normal and strike-slip faults (8–12 in Fig. 7c and d). West of the indenter, new normal faults accommodate the extensional component of deformation which further contributes to basin enlargement (13 in Fig. 7c and d).

Towards the end of the experiment, the basin system expands, especially to the west of the main strike-slip zone where new faults (14 and 15 in Fig. 7e and f) accommodate subsidence at the transition from extension in the north to strike-slip and the extension in the west. North of the indenter, the structure of the basin is characterized by sub-basins separated by intra-basinal highs (cross-section a-a' in Fig. 7g). In the area around the NW corner of the indenter where the two extension directions interfere, the structural pattern is more complex (Fig. 7e and cross-section b-b' in Fig. 7g). In this area, strain is partitioned into extension-dominated and strike-slip-dominated regions (areas of blue and green in Fig. 7f). A distinct feature is a narrow zone of shortening to transpressional deformation located in the hanging wall of fault 3, which can be inferred from the strain analysis (Fig. 7f), but cannot be seen in cross-sections (i.e., no reverse displacement in cross-sections a-a' and b-b' in Fig. 7g). In our view, this feature is probably an artefact of PIV analysis and is related to rotation of the hanging wall of fault 3 (or footwall of fault 7; see cross-sections a-a' and b-b' in Fig. 7g). This block rotates (clockwise in sections a-a' and b-b' in Fig. 7g) around a horizontal axis due to the listric geometry of fault 3 (Fig. 7h). While the entire block moves away from the indenter due to extension, the rotation brings the segment of this block located away from fault 3 up and to-wards the footwall (Fig. 7h). In map view such displacement creates local apparent shortening (Fig. 7h). A similar, but less expressed, feature can be observed also in the model 2 above the fault 3 (Fig. 5). Towards the south, the basin narrows significantly (Fig. 7e and cross-section c-c' in Fig. 7g) until the strike-slip deformation starts its transfer to trans-pression and creates a positive topography (cross-section d-d' in Fig. 7g). The main strike-slip fault system (1, 2 and 9 in Fig. 7e and f) propagates south-wards (16 in Fig. 7e and f and cross-section d-d' in Fig. 7g) and overprints the thrust wedge.

5. Effects of extension(s) on strain partitioning and deformation transfer around an indenter

The previous study of Krstekanić et al. (2021) has shown that deformation transfer during indentation without an additional exter-nally driven extension is controlled mainly by the geometry of the indenter. The new modelling results of this study exhibit similar features to Krstekanić et al. (2021) for similar modelling setups (model 1) but differ for areas which are affected by extensional boundary conditions (models 2–4). All models show similar deformation patterns with the formation of a thrust wedge (overprinted by low-offset normal faulting due to gravitational collapse; compare cross-section c-c' in Fig. 4g, cross-section e-e' in Fig. 5g, cross-section d-d' in Fig. 6g and cross-section e-e' in Fig. 7g) with almost similar topographic height (4.4
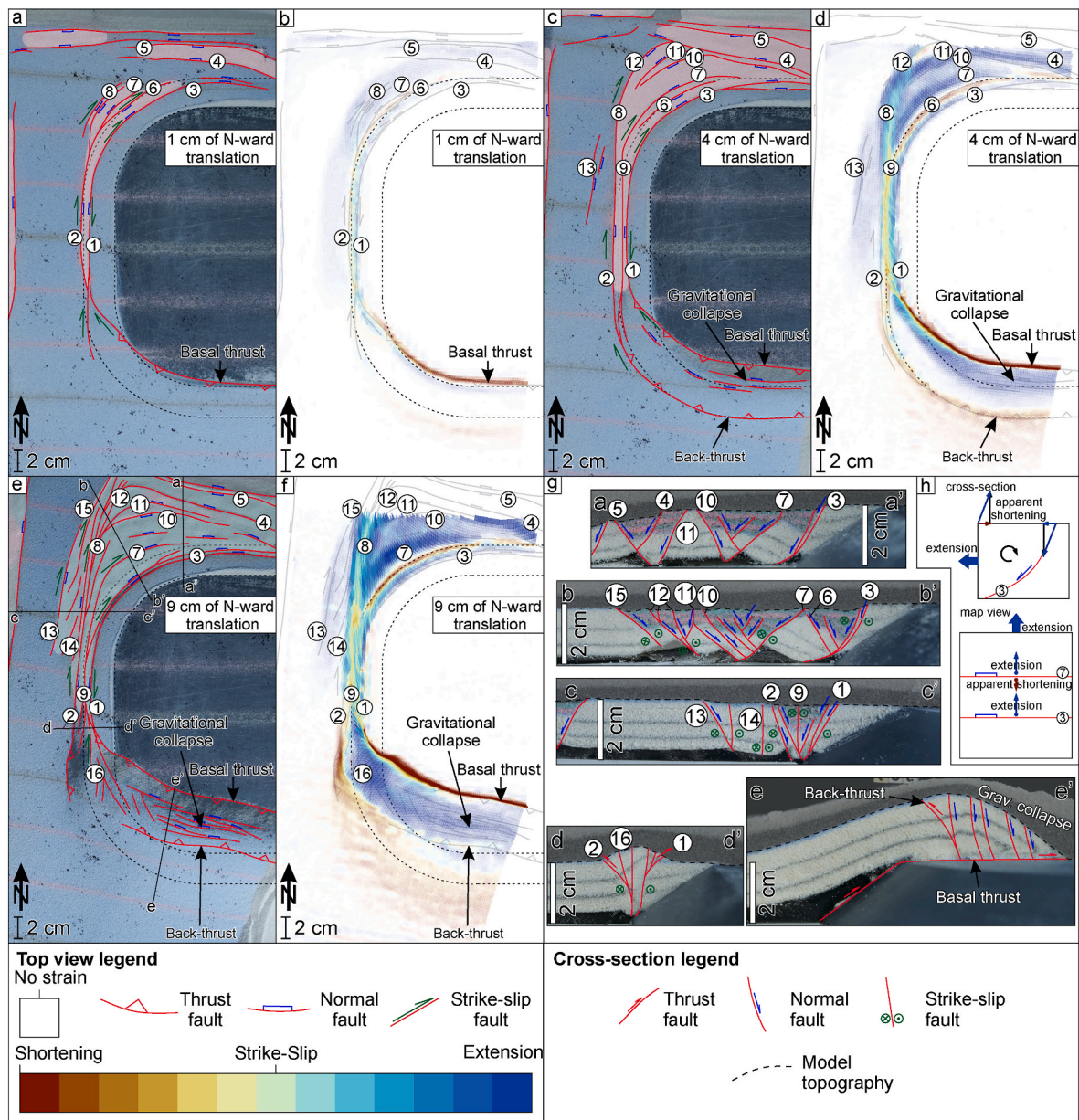
Fig. 7. Model 4 - open northern and partially open western boundaries. Dashed black lines mark the upper and lower edges of the indenter. R – Riedel shear. Highlighted semi-transparent white area marks the location of basin(s) with sedimentary infill. a) Interpreted top-view photo after 1 cm of northward translation. b) Cumulative average strain type map after 1 cm of northward translation. c) Interpreted top-view photo after 4 cm of northward translation. d) Cumulative average strain type map after 4 cm of northward translation. e) Interpreted top-view photo at the end of the experiment. f) Cumulative average strain type map at the end of the experiment. Strain plots in Fig. 7b, d and f overlay visually interpreted structures from Fig. 7a, c and e (grey lines). Strain colour legend corresponds to Fig. 7b, d and f. Note that in order to suppress areas without significant deformation, the transparency of areas with a strain magnitude below the 90 percentile is increased. g) Cross-sections of the reference model at the end of the experiment. Dashed line marks the model topography at the end of the experiment. Shaded area in the upper part of each cross-section marks post-kinematic sand cover. Cross-section locations are shown in Fig. 7e h) Cross-section and map view sketches of hanging wall kinematics above a listric normal fault that leads to an apparent shortening in PIV strain analysis. (For interpretation of the references to colour in this figure legend, the reader is referred to the Web version of this article.)

cm, 4.3 cm, 4.1 cm and 4.3 cm for models 1–4, respectively) in the south and its transition to transpression and strike-slip south-west of the indenter (Figs. 4–7). This suggests that extension imposed on the north-western and northern model boundary did not affect the deformation at the southern and south-western model areas. In contrast, significant subsidence associated with transtension and normal faulting creating isolated or connected basins is observed along the northern, north-western and western indenter's margins in models that allow extension at their margins (models 2–4, Figs. 5–7).

This extension and resulting subsidence are driven by the flow of the viscous layer in the direction of the free margin(s). Such flow of the viscous substratum underneath the brittle overburden is always a combination of a Poiseuille (the largest flow velocity in the middle of the viscous layer) and a Couette (the flow velocity in the viscous layer increases upwards) flows (Gemmer et al., 2004, 2005). With the progress of extension and the formation of the sedimentary basins, the effect of the Couette flow increases in the area beneath the sedimentary basins compared to the Poiseuille flow (Krézsek et al., 2007). This leads to the thinning of, and in cases of extreme extension, to breaking of the viscous layer. Effects of the viscous flow velocities on the model evolution are

related to the rheological and geometrical characteristics of the model layers (Weijermars et al., 1993; Gemmer et al., 2004, 2005; Krézsek et al., 2007; Brun and Fort, 2011). In our models, we do not vary the rheology and initial thickness of our model layers and add syn-kinematic sediments in the same way (see section 3.3) in all models. Therefore, we consider that observed structural differences in our models are not related to the variability of the viscous flow velocities, but the general

flow direction.

5.1. The influence of the northern extension

Extension along the northern boundary creates a NNE to ENE oriented displacement field in the area north of the indenter (Fig. 8a) resulting in a large basin with a curved southern margin, controlled by
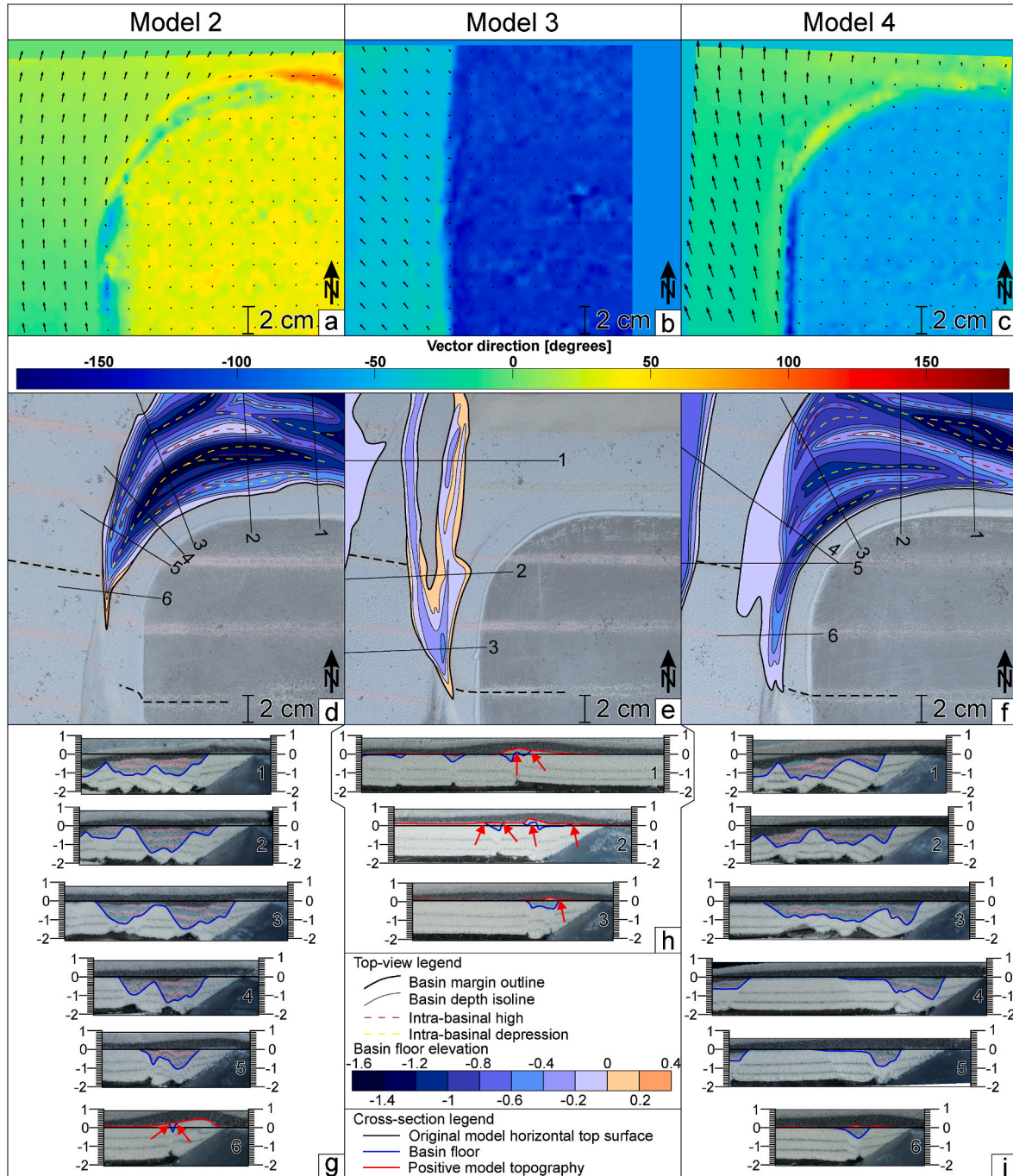

Fig. 8. a-c) Incremental displacement directions after 1 cm of total displacement in the northern halves of models 2, 3 and 4, respectively. Black arrow length indicates relative displacement magnitude. When there is no displacement (e.g., area of indenter) vector direction is randomly assigned by the software and is irrelevant in analysis. In the displacement vector direction legend, 0 is equivalent of north, −90 is west, while 90 is east. d-f) Final top-view photographs of northern parts of models 2, 3 and 4, respectively, overlain by structural maps of the basin floor. Dashed black line indicates the location of the central passive marker line on the model surface. Cross-sections locations are indicated by straight black lines and respective numbers. The maps are constructed by measuring elevation of basin floor in the cross-sections (g–i), projecting them in top-views along the respective cross-section lines and interpolating isolines in the areas between cross-sections. Isolines are drawn at 0.2 cm vertical distance. Red arrows in the cross-sections point to basin floor that is elevated above the original flat surface of the model. (For interpretation of the references to colour in this figure legend, the reader is referred to the Web version of this article.)

the geometry of the indenter's NW corner. West-wards, the basin is bound by a strike-slip to transtensional fault system (Figs. 5e and 8d) that has numerous splays curved to the east, along which the connection with normal faulting is ultimately established. The extension evolves gradually, which results in a segmented basin that has several elongated depo-centres (yellow dashed lines in Fig. 8d), separated by intra-basinal highs of different elevation (red dashed lines in Fig. 8d; see also cross-sections in Fig. 8g). The largest basin depth is observed in the vicinity of the NW indenter's corner, reaching 1.5 cm (cross-sections 2 and 3 in Fig. 8g). South-wards, the basin narrows and becomes less deep, as the influence of the north-ward extension decreases. The southern tip of the basin is located at the transition of the curved NW corner to the straight N–S oriented indenter's margin. This is the area where the main strike-slip deformation changes its kinematics, from transtension in the north to transpression in the south, while inverting the basin at the same time. This inversion results in the positive topography of the model and uplift of the basin floor (the elevation of the basin floor is, locally, higher than the original model surface in Fig. 8d; red arrows in cross-section 6 in Fig. 8g).

5.2. The influence of the western extension

West-ward directed gravity spreading along the western model boundary combined with the north-ward motor-induced pull create a displacement field oriented towards NW (Fig. 8b), which distributes strike-slip deformation west-wards and adds a transtensional component. Such coupled strike-slip and extension partition the deformation in two elongated ~ N–S oriented transtensional corridors that control basin formation (Fig. 8e). These elongate basins merge south-wards and reach up to the centre of the N–S oriented western margin of the indenter (marked by the dashed black marker line in Fig. 8e). With the cessation of the western extension, the strike-slip deformation takes over, inverting the basins, especially the one along the main eastern strike-slip corridor (Fig. 8e). This inversion is observed by uplift of the basin infill and its deformed floor (cross-sections in Fig. 8h), which implies that the relatively shallow basin system (less than 0.5 cm depth; see cross-section 3 in Fig. 8h) was deeper before inversion.

5.3. The influence of the coeval and coupled bi-directional extensions

When extension is bi-directional, the influence of extension along the northern boundary dominates over that along the western boundary, because more extension is applied along the former. The early model displacements are oriented to the NNW in the west, which changes to NE in the east (Fig. 8c). Similar to the model 2 (Fig. 8d), the northern extension creates a large basin with a curved southern margin and numerous elongated sub-basins and intra-basinal highs (Fig. 8f). These sub-basins are, in top-view, more often dissected, less continuous and wider towards the west when compared with model 2 (compare Fig. 8d with 8f). This is due to the north-west-ward flow of the silicone that distributes deformation over a wider area (compare Fig. 8a with 8c). The basin extends farther south-wards where the tip of the basin reaches central regions of the western indenter's margin, similar to model 3 (compare Fig. 8e with 8f). The basin reaches 1.3 cm depth (cross-sections 1 and 3 in Fig. 8i), which is ~13% less when compared with model 2, where the basin was about 1.5 cm deep, which indicates an extension and associated subsidence distributed over a larger area. The southern tip of the basin was likely inverted, which is suggested by the associated uplift resulting in positive basin infill topography (cross-section 6 in Fig. 8i). This inversion is the largest in the model with only northward extension and is lowest in the case when both extensions are present in the model (compare cross-sections 6 in Figs. 8g, 2 and 3 in Figs. 8h and 6 in Fig. 8i). Therefore, the northern extension controls the opening of a wider basin, the internal distribution of fault offsets, subsidence and the connection to the curved strike-slip faulting along the western indenter's margin. The west-ward extension creates a transtensional deformation

regime with subsidence along N–S oriented strike-slip faults, pulling and distributing the deformation towards the west, allowing for an additional, but relatively minor amount of subsidence west of the indenter.

5.4. Implications for the indentation processes

Existing modelling studies that investigate indentation and resulting shortening indicate that lateral extrusion during indentation requires a weaker crust and/or lithosphere rheology to be present laterally in the system (e.g., Ratschbacher et al., 1991a; Sokoutis et al., 2000; Rosenberg et al., 2004; van Gelder et al., 2017), associated or not with extension driven by slab roll-back (e.g., Faccenna et al., 1996; Philippon et al., 2014; Schellart et al., 2019) and sometimes coupled with a collapse and spreading of orogenic wedges (Faccenna et al., 1996; Kydonakis et al., 2015). When the lateral margins are confined, there is no lateral extrusion and deformation is transferred only around the indenter and partitioned between shortening, transpression and strike-slip deformation depending on the indenter geometry (Zweigel 1998; Luth et al., 2013; Schellart et al., 2019; Krstekanić et al., 2021). These results imply that a form of extension or gravity spreading at a high angle to indentation shortening along one or multiple margins of the system is essential for lateral extrusion in indentation systems. Our models are in agreement with these previous inferences, but further imply that the amount of extension and thus space generated by this process is critical for lateral extrusion to occur. In cases of limited externally-driven extension, the structural complexity increases by adding an extensional component to indentation-induced deformation, but it will not lead to large-scale extrusion of fault-bound crustal blocks.

6. Implications for the evolution of the Carpatho-Balkanides

The Circum-Moesian Fault System associated with the Carpatho-Balkanides backarc-convex oroclinal bending partitions the deformation around the Moesian Platform indenter in a similar way as in our analogue models, from transtension and strike-slip to transpression and shortening (Figs. 2 and 9; Krstekanić et al., 2020, 2021, 2022). This deformation was coeval with roll-back of the Carpathian embayment and Adriatic slabs that together created the observed bimodal back-arc extension (Fig. 9; see also Matenco and Radivojević, 2012).

Our models suggest that the extension and transtension north and north-west of the indenter can be indeed explained by the bimodal N–S and E-W oriented extension. The roll-back of the Carpathian embayment slab pulled its upper plate creating the orogen-parallel N–S, NE-SW to ENE-WSW oriented extension in the Serbian and South Carpathians and their foreland due to the corner effect of Moesia (e.g., Schmid et al., 1998; Matenco and Schmid, 1999; Ratschbacher et al., 1993; Krstekanić et al., 2020). Previous studies have shown 4–6 km of maximum Oligocene - early Miocene subsidence in various locations within the Getic Depression (e.g., Matenco et al., 2003; Răbăgia et al., 2011; Krézsek et al., 2013), which is smaller when compared with our models (1.3–1.5 cm in models scale to ~10 km in nature). Owing to the subsequent post-early Miocene basin inversion and burial to large depths (~10 km) in the proximity of the South Carpathians, these studies were not able to establish a very precise internal geometry of the Oligocene - Early Miocene basin beyond a potential separation in northern and southern sub-basins by an intermediary high (e.g., Fig. 1b in Răbăgia et al., 2011 or Fig. 7 in Krézsek et al., 2013), which connect gradually to the west and SW in the present-day geometry. Our bi-modal extension results (Fig. 8f) predict a similar geometry and furthermore suggest that the Oligocene - early Miocene sediment thicknesses are similar in transects across sub-basins, but with higher northern values in the central Getic Depression. Although the detailed fault geometry and distribution is somewhat different, the deformation transfer and interplay between Timok Fault strike-slip offset to N- to NE-wards transtension and further east-wards normal faulting in the Getic Depression shows clear resemblance with our north and bi-modal extension models (see Răbăgia and
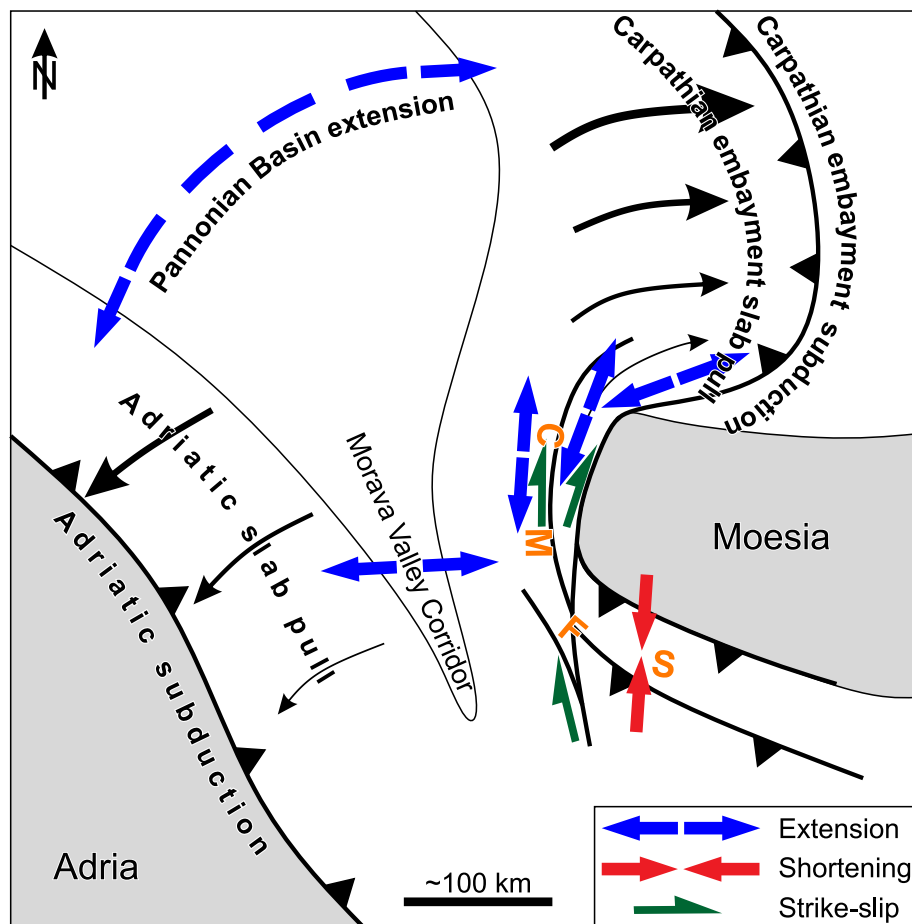
Fig. 9. Sketch of the influence of Carpathian embayment and Adriatic slabs on the deformation around the Moesian Platform. Both slab roll-backs exert pull on the upper plate, which results in the extension in the Pannonian Basin. Additionally, Carpathian embayment slab pull creates orogen-parallel extension along the Moesian indenter, which changes its orientation around the NW corner of Moesia and is, thus directed in ENE-WSW to N–W direction. To the west of the Moesia the extension in the Morava Valley Corridor is produced by the Adriatic slab pull and is perpendicular to the Moesian western margin. Both extensions affect the transfer of deformation in the Circum-Moesian Fault System (CMFS, orange letters) that is made of several thrusts south of Moesia and strike-slip deformation along the Moesian western margin. (For interpretation of the references to colour in this figure legend, the reader is referred to the Web version of this article.)

Maţenco, 1999; Krézsek et al., 2013).

The size of the modelled basins, which reflects the combined effect of extension and strike-slip faulting, is for several reasons exaggerated when compared to the Getic Depression. Most importantly, extension rates are exaggerated in our models, which are, though smaller than the strike-slip rates, higher than extension rates in the natural case. At the same time, the contribution of the strike-slip deformation in the Getic Depression is higher in the natural case than in our models (e.g., Schmid et al., 2008, and references therein). Furthermore, we note that the position of the pole of rotation, which has been chosen following regional kinematic reconstructions and available paleomagnetic studies (e.g., Balla, 1987; Fügenschuh and Schmid, S.M., 2005; Panaiotu and Panaiotu, 2010; van Hinsbergen et al., 2020), also impacts the amount of extension as a function of distance from the rotation pole. Our models do not account for pre-existing topography at the onset of basin formation in the South Carpathians (e.g., Moser et al., 2005), which directly impacts on the size of the resulting basins. In the natural case, the interplay of strike-slip and extension/transtension was distributed not only in the Getic Depression but also in the central and western part of the South Carpathians, where transtensional and extensional basins, such as the Petroşani, Caransebeş-Mehadia and Bozovici basins (Fig. 2b) formed during Oligocene - middle Miocene and are controlled by interacting strike-slip and normal faults, both orogen-parralel and orogen-perpendicular (e.g., Ratschbacher et al., 1993; Linzer et al., 1998; Matenco and Schmid, 1999; Codrea, 2001; Moser et al., 2005; Hír et al., 2016). Furthermore, the coeval interplay between strike-slip and normal faulting led to renewed deposition in the earlier formed Late Cretaceous Haţeg Basin of the South Carpathians (Linzer et al., 1998, and references therein). Nevertheless, these natural observations are also reflected in our models showing that transtensional/extensional

deformation affected a larger area than the present-day Getic Depression.

The geometry of the extension along the western model margin is very similar to the one of the orogen-perpendicular extension in the Morava Valley Corridor, which is probably driven by the Adriatic slab roll-back, affecting only the hinge area of the Carpatho-Balkanides back-arc convex orocline (Figs. 2 and 9, the westernmost side of the Serbian Carpathians bordering the Morava Valley Corridor, Matenco and Radivojević, 2012; Erak et al., 2017; Sant et al., 2018; Krstekanić et al., 2020). This Oligocene - Miocene orogen-perpendicular extension decreases gradually E– and S- wards (Krstekanić et al., 2020), while extending with time during the middle Miocene to the SW into the external Dinarides (Andrić et al., 2018; van Unen et al., 2019 and references therein). Our modelling results show that the west-ward extension allows for the partitioning of strike-slip deformation into multiple sub-parallel strike-slip faults that merge into a single deformation zone along the western margin of the indenter. The connecting geometry and observed west-ward continuation of the orogen perpendicular extension is realistic in the model with bimodal extension when compared with the observed fault geometry and splaying characteristics (compare Fig. 2b with Figs. 7e and 8f, e.g., splaying the Timok offset along the Sokobanja-Zvonce and Rtanj-Pirot faults in Fig. 2b). These observations infer that the geometry of the Circum-Moesian Fault System requires the Morava Valley extension to be coupled with the oroclinal bending and orogen-parallel extension. The shallow (<1 km) E-W oriented intra-montane basins of the Serbian Carpathians (Fig. 2) were not reproduced by our modelling, possibly because of the limited gravity spreading created at the margins of our model, which does not completely reproduce the likely larger horizontal forces exerted by a slab roll-back, remaining a feature for further study.

7. Conclusions

We studied the effects of externally driven extension on strain partitioning and deformation transfer around an indenter by the means of analogue modelling. We have built four crustal scale analogue models where the deformable crust is translated and rotated around a stationary rigid indenter, while the externally driven extension is simulated by allowing the viscous layer to flow in directions parallel and perpendicular to the indenter margins. This allowed a quantitative assessment of the effects of superposed extension on the evolution of a strike-slip dominated deformation zone during indentation.

Previous studies have shown that the indenter geometry controls the style of deformation and that strike-slip at the margin of the indenter is gradually connected to shortening in its frontal part. Our modelling results show that the additional extension with a direction parallel to the strike-slip zone is responsible for the opening of a large sedimentary basin behind the indenter, characterised by sub-basins and intra-basinal highs, which are controlled by strain partitioning between the curved strike-slip, transtensional and normal faults. Furthermore, this extension stimulates an increase in the strike-slip faults curvature by connecting them with the basin-controlling normal faults. The extension perpendicular to the strike-slip system distributes deformation away from the indenter, creating a strike-slip system splaying into two zones of transtensional to strike-slip deformation that connect in the south and accommodate additional minor subsidence along N–S oriented transtensional faults. The modelling furthermore shows that bi-modal parallel and perpendicular extension controls the first-order structure and extent (west-ward and south-ward) of the subsidence in the basin.

The modelling results infer that the Circum-Moesian Fault System was affected by extensions in different directions driven by the Carpathian embayment and Adriatic slab roll-backs. The extension in the north opened the Getic Depression, partitioned the strike-slip deformation and increased the curvature of the large Cerna and Timok faults and connected them with normal faults. The west-ward pull of the Adriatic slab added a component of transtensional deformation to the strike-slip system during the indentation by the Moesian Platform and contributed to splaying strike-slip deformation west-wards.

Our modelling results demonstrate that the deformation transfer around rigid indenters can be significantly affected by far-field extension involving enhanced subsidence in newly formed basins, distributing deformation over a wider area and increasing in oblique kinematics along differently oriented faults, which create complex strain partitioning patterns.

Data availability

All raw unprocessed data related to this study are deposited in the Yoda data repository system of Utrecht University with the DOI number 10.24416/UU01–N7TDVH and can be accessed via: https://public.yoda.uu.nl/geo/UU01/N7TDVH.html. Further information is available by contacting the corresponding author or the TecLab (teclab.geo@uu.nl).

CRediT authorship contribution statement

Nemanja Krstekanić: Conceptualization, Methodology, Validation, Formal analysis, Investigation, Data curation, Writing – original draft, Writing – review & editing, Visualization. **Ernst Willingshofer:** Conceptualization, Methodology, Validation, Resources, Writing – original draft, Writing – review & editing, Supervision. **Liviu Matenco:** Writing – original draft, Writing – review & editing, Supervision. **Marinko Toljić:** Supervision, Writing – review & editing. **Uros Stojadinovic:** Supervision, Writing – review & editing.

Declaration of competing interest

The authors declare that they have no known competing financial interests or personal relationships that could have appeared to influence the work reported in this paper.

Appendix A. Supplementary data

Supplementary data to this article can be found online at https://doi.org/10.1016/j.jsg.2022.104599.

References

Andrić, N., Vogt, K., Matenco, L., Cvetković, V., Cloetingh, S., Gerya, T., 2018. Variability of orogenic magmatism during Mediterranean-style continental collisions: a numerical modelling approach. Gondwana Res. 56, 119–134.

Balla, Z., 1987. Tertiary palaeomagnetic data for the Carpatho–Pannonian region in the light of Miocene rotation kinematics. Tectonophysics 139, 67–98.

Benesh, N.P., Plesch, A., Shaw, J.H., 2014. Geometry, kinematics, and displacement characteristics of tear-fault systems: an example from the deep-water Niger Delta. AAPG (Am. Assoc. Pet. Geol.) Bull. 98 (3), 465–482.

Bennett, R.A., Hreinsdóttir, S., Buble, G., Bašić, T., Bačić, Ž., Marjanović, M., Casale, G., Gendaszek, A., Cowan, D., 2008. Eocene to present subduction of southern Adria mantle lithosphere beneath the Dinarides. Geology 36 (1), 3–6.

Berza, T., Drăgănescu, A., 1988. The Cerna–Jiu fault system (South Carpathians, Romania), a major Tertiary transcurrent lineament. DS Inst. Geol. Geofiz. 72– 73, 43–57.

Broerse, T., 2021. Tacobroerse/Strainmap: v1.0 (v1.0). Zenodo. https://doi.org/10.5281/zenodo.4529475.

Broerse, T., Krstekanić, N., Kasbergen, C., Willingshofer, E., 2021. Mapping and classifying large deformation from digital imagery: application to analogue models of lithosphere deformation. Geophys. J. Int. 226, 984–1017.

Brun, J.-P., 2002. Deformation of the continental lithosphere: insights from brittle-ductile models. Geological Society, London, Special Publications 200, 355–370.

Brun, J.-P., Fort, X., 2004. Compressional salt tectonics (Angolan margin). Tectonophysics 382, 129–150.

Brun, J.-P., Fort, X., 2011. Salt tectonics at passive margins: Geology versus models. Mar. Petrol. Geol. 28, 1123–1145.

Cembrano, J., González, G., Arancibia, G., Ahumada, I., Olivares, V., Herrera, V., 2005. Fault zone development and strain partitioning in an extensional strike-slip duplex: a case study from the Mesozoic Atacama fault system, Northern Chile. Tectonophysics 400, 105–125.

Cobbold, P.R., Szatmari, P., 1991. Radial gravitational gliding on passive margins. Tectonophysics 188, 249–289.

Codrea, V.A., 2001. Badenian insectivores from Bozovici basin (southern Carpathians, caraş-severin district). Acta Paleontologica Romaniae V (3), 67–75.

Csontos, L., Vörös, A., 2004. Mesozoic plate tectonic reconstruction of the Carpathian region. Palaeogeogr. Palaeoclimatol. Palaeoecol. 210, 1–56.

Davy, P., Cobbold, P.R., 1991. Experiments on shortening of a 4-layer model of the continental lithosphere. Tectonophysics 188, 1–25.

D'el-Rey Silva, L.J.H., de Oliveira, Í.L., Pohren, C.B., Tanizaki, M.L.N., Carneiro, R.C., Fernandes, G.L. de F., Aragão, P.E., 2011. Coeval perpendicular shortenings in the Brasília belt: collision of irregular plate margins leading to oroclinal bending in the Neoproterozoic of central Brazil. J. S. Am. Earth Sci. 32, 1–13.

De Vicente, G., Regas, R., Muñoz-Martín, A., Van Wees, J.D., Casas-Sáinz, A., Sopeña, A., Sánchez-Moya, P., Arche, A., López-Gómez, J., Oláiz, A., Fernandez Lozano, J., 2009. Oblique strain partitioning and transpression on an inverted rift: the Castilian Branch of the Iberian Chain. Tectonophysics 470, 224–242.

Dimitrijevic, M.D. (Ed.), 1994. Geological Atlas of Serbia 1:2.000.000. Seismotectonic and Seismological Map, vol. 1994. Republic Foundation for Geological Investigations and Geological Institute GEMINI, Belgrade.

Erak, D., Matenco, L., Toljić, M., Stojadinović, U., Andriessen, P.A.M., Willingshofer, E., Ducea, M.N., 2017. From nappe stacking to extensional detachments at the contact between the Carpathians and Dinarides – the Jastrebac Mountains of Central Serbia. Tectonophysics 710– 711, 162–183.

Faccenna, C., Davy, P., Brun, J.-P., Funiciello, R., Giardini, D., Mattei, M., Nalpas, T., 1996. The dynamics of back-arc extension: an experimental approach to the opening of the Tyrrhenian Sea. Geophys. J. Int. 126, 781–795.

Frisch, W., Kuhlemann, J., Dunkl, I., Brügel, A., 1998. Palinspastic reconstruction and topographic evolution of the Eastern Alps during late Tertiary tectonic extrusion. Tectonophysics 297, 1–15.

Fügenschuh, B., Schmid, S.M., 2005. Age and significance of core complex formation in a very curved orogen: evidence from fission track studies in the South Carpathians (Romania). Tectonophysics 404, 33–53.

Gemmer, L., Ings, S.J., Medvedev, S., Beaumont, C., 2004. Salt tectonics driven by differential sediment loading: stability analysis and finite-element experiments. Basin Res. 16, 99–218.

Gemmer, L., Beaumont, C., Ings, S.J., 2005. Dynamic modelling of passive margin salt tectonics: effects of water loading, sediment properties and sedimentation patterns. Basin Res. 17, 383–402.

Glen, J.M.G., 2004. A kinematic model for the southern Alaska orocline based on regional fault patterns. In: Sussman, A.J., Weil, A.B. (Eds.), Orogenic Curvature: Integrating Paleomagnetic and Structural Analyses: Geological Society of America Special Paper 383. Geological Society of America, Boulder, CO, pp. 161–172.

Govers, R., Wortel, M.J.R., 2005. Lithosphere tearing at STEP faults: response to edges of subduction zones. Earth Planet Sci. Lett. 236, 505–523.

Hír, J., Venczel, M., Codrea, V., Angelone, C., van den Hoek Otende, L.W., Kirscher, U., Prieto, J., 2016. Badenian and Sarmatian s.str. from the Carpathian area: overview and ongoing research on Hungarian and Romanian small vertebrate evolution. Comptes Rendus Palevol 15, 863–875.

Horváth, F., Musitz, B., Balázs, A., Végh, A., Uhrin, A., Nádor, A., Koroknai, B., Pap, N., Tóth, T., Wórum, G., 2015. Evolution of the Pannonian basin and its geothermal resources. Geothermics 53, 328–352.

Hubbert, M.K., 1937. Theory of scale models as applied to the study of geologic structures. GSA Bulletin 48 (10), 1459–1520.

Kaymakci, N., Inceöz, M., Ertepinar, P., Koç, A., 2010. Late cretaceous to recent kinematics of SE Anatolia (Turkey). In: Sosson, M., Kaymakci, N., Stephenson, R.A., Bergerat, F., Starostenko, V. (Eds.), Sedimentary Basin Tectonics from the Black Sea and Caucasus to the Arabian Platform, vol. 340. Geological Society, London, Special Publications, pp. 409–435.

Kräutner, H.G., Krstić, B., 2002. Alpine and pre-Alpine structural units within southern Carpathians and the eastern Balkanides. In: Proceedings of XVII Congress of Carpathian–Balkan Geological Association, Geologica Carpathica, vol. 53. Special Issue.

Kräutner, H.G., Krstić, B., 2003. Geological Map of the Carpatho–Balkanides between Mehadia, Oravița, Niš and Sofia. Geoinstitute, Belgrade.

Krézsek, C., Adam, J., Grujic, D., 2007. Mechanics of fault and expulsion rollover systems developed on passive margins detached on salt: insights from analogue modelling and optical strain monitoring. Geological Society, London, Special Publications 292, 103–121.

Krézsek, C., Lăpădat, A., Mațenco, L., Arnberger, K., Barbu, V., Olaru, R., 2013. Strain partitioning at orogenic contacts during rotation, strike-slip and oblique convergence: paleogene–Early Miocene evolution of the contact between the South Carpathians and Moesia. Global Planet. Change 103, 63–81.

Krstekanić, N., Matenco, L., Toljić, M., Mandić, O., Stojadinović, U., Willingshofer, E., 2020. Understanding partitioning of deformation in highly arcuate orogenic systems: inferences from the evolution of the South Carpathians. Global Planet. Change. https://doi.org/10.1016/j.gloplacha.2020.103361.

Krstekanić, N., Willingshofer, E., Broerse, T., Matenco, L., Toljić, M., Stojadinovic, U., 2021. Analogue modelling of strain partitioning along a curved strike-slip fault system during backarc-convex orocline formation: implications for the Cerna-Timok fault system of the Carpatho-Balkanides. J. Struct. Geol. 149, 104386 https://doi.org/10.1016/j.jsg.2021.104386.

Krstekanić, N., Matenco, L., Stojadinovic, U., Willingshofer, E., Toljić, M., Tamminga, D., 2022. Strain partitioning in a large intracontinental strike-slip system accommodating backarc-convex orocline formation: the Circum-Moesian Fault System of the Carpatho-Balkanides. Global Planet. Change 208, 103714. https://doi.org/10.1016/j.gloplacha.2021.103714.

Kydonakis, K., Brun, J.-P., Sokoutis, D., 2015. North Aegean core complexes, the gravity spreading of a thrust wedge. J. Geophys. Res. Solid Earth 120, 595–616.

Linzer, H.-G., Frisch, W., Zweigel, P., Girbacea, R., Hann, H.-P., Moser, F., 1998. Kinematic evolution of the Romanian Carpathians. Tectonophysics 297, 133–156.

Luth, S., Willingshofer, E., ter Borgh, M., Sokoutis, D., van Otterloo, J., Versteeg, A., 2013. Kinematic and analogue modelling of the Passier- and Jaufen faults: implications for crustal indentation in the Eastern Alps. Int. J. Earth Sci. 102, 1071–1090.

Lyberis, N., Yurur, T., Chorowicz, J., Kasapoglu, E., Gundogdu, N., 1992. The East Anatolian Fault: an oblique collisional belt. Tectonophysics 204, 1–15.

Mantovani, E., Viti, M., Babbucci, D., Tamburelli, C., Albarello, D., 2006. Geodynamic connection between the indentation of Arabia and the Neogene tectonics of the central–eastern Mediterranean region. In: Dilek, Y., Pavlides, S. (Eds.), Postcollisional Tectonics and Magmatism in the Mediterranean Region and Asia, vol. 409. Geological Society of America Special Paper, pp. 15–41.

Martinod, J., Hatzfeld, D., Brun, J.P., Davy, P., Gautier, P., 2000. Continental collision, gravity spreading, and kinematics of Aegea and Anatolia. Tectonics 19 (2), 290–299.

Mațenco, L., 2017. Tectonics and exhumation of Romanian Carpathians: inferences from kinematic and thermochronological studies. In: Rădoane, M., Vespremeanu-Stroe, A. (Eds.), Landform Dynamics and Evolution in Romania. Springer Geography. Springer, pp. 15–56.

Matenco, L., Radivojević, D., 2012. On the formation and evolution of the Pannonian Basin: constraints derived from the structure of the junction area between the Carpathians and Dinarides. Tectonics 31, TC6007. https://doi.org/10.1029/2012TC003206.

Matenco, L., Schmid, S., 1999. Exhumation of the Danubian nappes system (South Carpathians) during the Early Tertiary: inferences from kinematic and paleostress analysis at the Getic/Danubian nappes contact. Tectonophysics 314, 401–422.

Matenco, L., Bertotti, G., Cloetingh, S., Dinu, C., 2003. Subsidence analysis and tectonic evolution of the external Carpathian–Moesian Platform region during Neogene times. Sediment. Geol. 156, 71–94.

Molnar, P., Tapponier, P., 1975. Cenozoic tectonics of Asia: effects of a continental collision. Science 189 (4201), 419–426.

Moser, F., Hann, H.P., Dunkl, I., Frisch, W., 2005. Exhumation and relief history of the Southern Carpathians (Romania) as evaluated from apatite fission track chronology in crystalline basement and intramontane sedimentary rocks. Int. J. Earth Sci. 94, 218–230.

Morley, C.K., 2002. A tectonic model for the Tertiary evolution of strike–slip faults and rift basins in SE Asia. Tectonophysics 347, 189–215.

Morley, C.K., 2013. Discussion of tectonic models for Cenozoic strike–slip fault-affected continental margins of mainland SE Asia. J. Asian Earth Sci. 76, 137–151.

Neubauer, F., Fritz, H., Genser, J., Kurz, W., Nemes, F., Wallbrecher, E., Wang, X., Willingshofer, E., 2000. Structural evolution within an extruding wedge: model and application to the Alpine-Pannonian system. In: Lehner, F.K., Urai, J.L. (Eds.), Aspects of Tectonic Faulting (Festschrift in Honour of Georg Mandl). Springer-Verlag, Berlin – Heidelberg –, New York, pp. 141–153.

Panaiotu, C.G., Panaiotu, C.E., 2010. Palaeomagnetism of the upper cretaceous sânpetru formation (Hațeg Basin, South Carpathians). Palaeogeogr. Palaeoclimatol. Palaeoecol. 293, 343–352.

Perinçek, D., Çemen, İ., 1990. The structural relationship between the East Anatolian and Dead Sea fault zones in southeastern Turkey. Tectonophysics 172, 331–340.

Philippon, M., Brun, J.-P., Gueydan, F., Sokoutis, D., 2014. The interaction between Aegean back-arc extension and Anatolia escape since Middle Miocene. Tectonophysics 631, 176–188.

Popa, M., Munteanu, I., Borleanu, F., Oros, E., Radulian, M., Dinu, C., 2018. Active tectonic deformation and associated earthquakes: a case study – south West Carpathians Bend zone. Acta Geodaetica et Geophysica 53, 395–413.

Rabăgia, T., Mațenco, L., 1999. Tertiary tectonic and sedimentological evolution of the South Carpathians foredeep: tectonic vs eustatic control. Mar. Petrol. Geol. 16, 719–740.

Răbăgia, T., Matenco, L., Cloetingh, S., 2011. The interplay between eustacy, tectonics and surface processes during the growth of a fault-related structure as derived from sequence stratigraphy: the Govora–Ocnele Mari antiform, South Carpathians. Tectonophysics 502 (1–2), 196–220.

Ramberg, H., 1981. Gravity, Deformation, and the Earth's Crust: in Theory, Experiments, and Geological Application. Academic Press, London, New York.

Ratschbacher, L., Merle, O., Davy, P., Cobbold, P., 1991a. Lateral extrusion in the eastern Alps, Part 1: boundary conditions and experiments scaled for gravity. Tectonics 10 (2), 245–256.

Ratschbacher, L., Frisch, W., Linzer, H.-G., Merle, O., 1991b. Lateral extrusion in the eastern Alps, Part 2: structural analysis. Tectonics 10 (2), 257–271.

Ratschbacher, L., Linzer, H.G., Moser, F., Strusievicz, R.O., Bedelean, H., Har, N., Mogos, P.A., 1993. Cretaceous to Miocene thrusting and wrenching along the central South Carpathians due to a corner effect during collision and orocline formation. Tectonics 12, 855–873.

Regard, V., Faccenna, C., Martinod, J., Bellier, O., 2005. Slab pull and indentation tectonics: insights from 3D laboratory experiments. Phys. Earth Planet. In. 149, 99–113.

Rosenberg, C.L., Brun, J.-P., Gapais, D., 2004. Indentation model of the eastern Alps and the origin of the Tauern window. Geology 32 (11), 997–1000.

Rudolf, M., Boutelier, D., Rosenau, M., Schreurs, G., Oncken, O., 2016. Rheological benchmark of silicone oils used for analog modling of short- and longterm lithospheric deformation. Tectonophysics 684, 12–22.

Săndulescu, M., 1988. Cenozoic tectonic history of the Carpathians. In: Royden, L.H., Horvath, F. (Eds.), The Pannonian Basin, a Study in Basin Evolution, AAPG Memoir, vol. 45. American Association of Petroleum Geologists, Tulsa, OK, pp. 17–25.

Sant, K., Mandic, O., Rundić, Lj, Kuiper, K.F., Krijgsman, W., 2018. Age and evolution of the Serbian lake system: integrated results from middle Miocene lake popovac. Newsl. Stratigr. 51 (1), 117–143.

Schellart, W.P., Chen, Z., Strak, V., Duarte, J.C., Rosas, F.M., 2019. Pacific subduction control on Asian continental deformation including Tibetan extension and eastward extrusion tectonics. Nat. Commun. 10, 4480. https://doi.org/10.1038/s41467-019-12337-9.

Schmid, S.M., Berza, T., Diaconescu, V., Froitzheim, N., Fügenschuh, B., 1998. Orogen-parallel extension in the southern Carpathians. Tectonophysics 297, 209–228.

Schmid, S.M., Bernoulli, D., Fügenschuh, B., Matenco, L., Schefer, S., Schuster, R., Tischler, M., Ustaszewski, K., 2008. The Alpine–Carpathian–Dinaridic orogenic system: correlation and evolution of tectonic units. Swiss J. Geosci. 101, 139–183.

Schmid, S.M., Fügenschuh, B., Kounov, A., Matenco, L., Nievergelt, P., Oberhänsli, R., Pleuger, J., Schefer, S., Schuster, R., Tomljenović, B., Ustaszewski, K., van Hinsbergen, D.J.J., 2020. Tectonic units of the Alpine collision zone between Eastern Alps and western Turkey. Gondwana Res. 78, 308–374.

Searle, M.P., Elliot, J.R., Phillips, R.J., Chung, S.-L., 2011. Crustal–lithospheric structure and continental extrusion of Tibet. J. Geol. Soc. 168, 633–672.

Shen, F., Royden, L.H., Burchfiel, B.C., 2001. Large-scale crustal deformation of the Tibetan Plateau. J. Geophys. Res. 106 (B4), 6793–6816.

Smit, J., Brun, J.-P., Cloetingh, S., Ben-Avraham, Z., 2010. The rift-like structure and asymmetry of the Dead Sea Fault. Earth Planet Sci. Lett. 290, 74–82.

Sokoutis, D., Bonini, M., Medvedev, S., Boccaletti, M., Talbot, C.J., Koyi, H., 2000. Indentation of a continent with a built-in thickness change: experiment and nature. Tectonophysics 320, 243–270.

Sternai, P., Avouac, J.-P., Jolivet, L., Faccenna, C., Gerya, T., Becker, T.W., Menant, A., 2016. On the influence of the asthenospheric flow on the tectonics andtopography at a collision-subduction transition zones:Comparison with the eastern Tibetan margin. J. Geodyn. 100, 184–197.

Tapponnier, P., Peltzer, G., Aramijo, R., 1986. On the mechanics of the collision between India and Asia. In: Coward, M.P., Ries, A.C. (Eds.), Collision Tectonics, vol. 19. Geological Society Special Publication, pp. 115–157.

Thielicke, W., Stamhuis, E.J., 2014. PIVlab – towards user-friendly, Affordable and Accurate digital particle image velocimetry in MATLAB. J. Open Res. Software 2, e30. https://doi.org/10.5334/jors.bl.

Ustaszewski, K., Schmid, S.M., Fügenschuh, B., Tischler, M., Kissling, E., Spakman, W., 2008. A map-view restoration of the Alpine–carpathian–Dinaridic system for the early Miocene. Swiss J. Geosci. 101, 273–294.

van Gelder, I.E., Willingshofer, E., Sokoutis, D., Cloetingh, S.A.P.L., 2017. The interplay between subduction and lateral extrusion: a case study for the European Eastern Alps based on analogue models. Earth Planet Sci. Lett. 472, 82–94.

van Gelder, I.E., Willingshofer, E., Andriessen, P.A.M., Schuster, R., Sokoutis, D., 2020. Cooling and vertical motions of crustal wedges prior to, during, and after lateral extrusion in the eastern Alps: new field kinematic and fission track data from the Mur-Mürz fault system. Tectonics 39, e2019TC005754.

van Hinsbergen, D.J.J., Torsvik, T.H., Schmid, S.M., Maţenco, L.C., Maffione, M., Vissers, R.L.M., Gürer, D., Spakman, W., 2020. Orogenic architecture of the Mediterranean region and kinematic reconstruction of its tectonic evolution since the Triassic. Gondwana Res. 81, 79–229.

van Unen, M., Matenco, L., Demir, V., Nader, F.H., Darnault, R., Mandić, O., 2019. Transfer of deformation during indentation: inferences from the post-middle Miocene evolution of the Dinarides. Global Planet. Change 182, 103027.

Warsitzka, M., Kley, J., Kukowski, N., 2015. Analogue experiments of salt flow and pillow growth due to basement faulting and differential loading. Solid Earth 6, 9–31.

Weijermars, R., Schmeling, H., 1986. Scaling of Newtonian and non-Newtonian fluid dynamics without inertia for quantitative modelling of rock flow due to gravity (including the concept of rheological similarity). Phys. Earth Planet. In. 43, 316–330.

Weijermars, R., Jackson, M.P.A., Vendeville, B., 1993. Rheological and tectonic modeling of salt provinces. Tectonophysics 217, 143–174.

Willingshofer, E., Sokoutis, D., Burg, J.-P., 2005. Lithospheric-scale analogue modelling of collision zones with a pre-existing weak zone. In: Gapais, D., Brun, J.P., Cobbold, P.R. (Eds.), Deformation Mechanisms, Rheology and Tectonics: from Minerals to the Lithosphere, ume 243. Geological Society, London, Special Publications, pp. 277–294, 243.

Willingshofer, E., Sokoutis, D., Beekman, F., Schönebeck, J.-M., Warsitzka, M., Rosenau, M., 2018. Ring Shear Test Data of Feldspar Sand and Quartz Sand Used in the Tectonic Laboratory (TecLab) at Utrecht University for Experimental Earth Science Applications. GFZ Data Services. https://doi.org/10.5880/fidgeo.2018.072.

Wölfler, A., Kurz, W., Fritz, H., Stüwe, K., 2011. Lateral extrusion in the Eastern Alps revisited: refining the model by thermochronological, sedimentary, and seismic data. Tectonics 30, TC4006. https://doi.org/10.1029/2010TC002782.

Zweigel, P., 1998. Arcuate accretionary wedge formation at convex plate margin corners: results of sandbox analogue experiments. J. Struct. Geol. 20 (12), 1597–1609.